Journal of Integrative Neuroscience

*J. Integr. Neurosci.* **2026**; 25(9): 53296
https://doi.org/10.31083/JIN53296

*Original Research*

# Mechanistic Study on HSP90B1 Regulation of ClC-7 Ubiquitination to Restore Lysosomal Function in the Protection Proffered by DGMI Against Fluoride-Induced Cognitive Dysfunction

Rui Chen[1,2,†], Peng Xie[3,†], Xinrui Fan[4], Zihang Zhou[4], Chunyan Mu[5,6], Qiuhong Ji[1,7,*]

[1]Suzhou Medical College of Soochow University, Soochow University, 215004 Suzhou, Jiangsu, China
[2]Department of Neurology, The Second People's Hospital of Huai'an and The Affiliated Huai'an Hospital of Xuzhou Medical University, 223001 Huai'an, Jiangsu, China
[3]Department of Neurosurgery, The Second People's Hospital of Huai'an and The Affiliated Huai'an Hospital of Xuzhou Medical University, 223001 Huai'an, Jiangsu, China
[4]Department of Neurobiology, Xuzhou Medical University, 221004 Xuzhou, Jiangsu, China
[5]Department of Psychiatry and Psychology, Xuzhou Medical University Affiliated Xuzhou Oriental Hospital, 221000 Xuzhou, Jiangsu, China
[6]The Key Laboratory of Psychiatry, Xuzhou Medical University, 221000 Xuzhou, Jiangsu, China
[7]Department of Neurology, The Affiliated Hospital of Nantong University, 226001 Nantong, Jiangsu, China
*Correspondence: jiqiuhong@ntu.edu.cn (Qiuhong Ji)
[†]These authors contributed equally.

Academic Editor: Changjong Moon
Submitted: 25 April 2026 Revised: 4 June 2026 Accepted: 9 June 2026 Published: 16 September 2026

**Abstract**

**Background:** Fluorosis can induce cognitive dysfunction. The cognitive impairment caused by fluorosis is closely related to endoplasmic reticulum stress (ERS) and abnormal lysosomal acidification. However, the specific molecular mechanism is not known, and effective intervention strategies are lacking. Diterpene ginkgolides meglumine injection (DGMI) is used clinically as a neuroprotective agent, but whether it can inhibit ERS, regulate lysosomal acidification, and ameliorate fluorosis-induced cognitive dysfunction merits investigation. **Methods:** We used the Morris water maze to detect the cognitive function of mice, evaluated the neuronal survival by Nissl staining, assessed the apoptotic status in hippocampal neurons of mice by terminal deoxynucleotidyl transferase dUTP nick-end labeling (TUNEL) staining, and observed the degree of synaptic plasticity damage using Golgi staining and transmission electron microscopy. In cell experiments, we used the OG488 acidophilic fluorescent probe to detect lysosomal acidity; detected the co-localization of HSP90B1 with the ER and the co-localization of the chloride channel, voltage-sensitive 7 (ClC-7) with lysosomes using immunofluorescence technology; employed co-immunoprecipitation to detect the binding of HSP90B1, ClC-7, and membrane-associated RING-CH protein 1 (MARCHF1) as well as the ubiquitination degradation level of ClC-7; used western blotting to measure expression of ERS-related proteins (PERK, IRE1α, ATF6), glycogen synthase kinase 3β, and mammalian target of rapamycin signals. **Results:** DGMI significantly improved cognitive dysfunction in C57BL/6 mice with fluorosis, inhibited hippocampal neuronal apoptosis, and improved synaptic plasticity damage. In cell experiments, the detection results of apoptosis and percent survival were consistent with those of animal experiments in that DGMI could alleviate sodium fluoride-induced ERS and lysosomal-acidification disorders in HT22 cells. DGMI downregulates the expression of the ER chaperone HSP90B1, weakens its interaction with ClC-7, thereby inhibiting the MARCHF1 E3 ligase-mediated ubiquitination and degradation of ClC-7, ultimately alleviating lysosomal acidification disorders and improving cognitive function. **Conclusions:** DGMI may exert cognitive protective effects against fluorosis-induced cognitive impairment by regulating lysosomal acidification through the HSP90B1–ClC-7 axis, which also alleviates ERS, apoptosis, and other related neuropathologic injuries.

**Keywords:** DGMI; HSP90B1; CIC-7; ubiquitination; endoplasmic reticulum stress; lysosomal acidification; cognitive dysfunction

## 1. Introduction

Fluoride is an inorganic, monatomic anion of fluorine, with the chemical formula $F^-$. It is an essential trace element for humans. Fluoride has a critical role in the development and mineralization of bones and teeth [1].

Naturally occurring fluoride is, in general, harmless. Health problems arise primarily in specific regions with abnormally high environmental fluoride concentrations, leading to chronic excessive intake and consequent disorders such as fluorosis (dental and skeletal) [2]. Numerous studies conducted in China and internationally have reported that children living in areas with high-fluoride drinking water have significantly lower average intelligence-quotient scores than children in control areas. Exposure to a high concentration of fluoride is associated with worse performance in executive functions (including attention, work-

ing memory, and processing speed) in children residing in fluorosis-endemic areas [3].

Emerging studies have focused on the mechanisms underlying fluoride neurotoxicity, including hippocampal neuronal apoptosis, oxidative stress, and neuroinflammation. However, effective approaches to identify and address the threats posed to human health, particularly targeted therapeutic drugs, are lacking [4]. Therefore, identifying the key toxic pathways and therapeutic agents for fluoride-induced neurotoxicity represents an urgent concern for public health.

Studies have demonstrated that fluoride can impair lysosomal function through multiple pathways: lysosomal Transient Receptor Potential Mucolipin 1 (TRPML1)/transcription factor EB (TFEB) axis inhibition-mediated autophagy dysregulation contributes to fluoride-induced neuronal damage [5]; fluoride activates the mammalian target of rapamycin (mTOR)C1/p-p70S6K signaling pathway, thereby inhibiting nuclear translocation of TFEB, leading to impairment of lysosomal biogenesis, accumulation of dysfunctional lysosomes, and subsequent disruption of autophagosome–lysosome fusion, ultimately compromising autophagic degradation [6]. These findings indicate that dysfunction of the lysosome–autophagy system represents a central mechanism in fluoride-induced neurotoxicity.

Lysosome function is strongly dependent upon the highly acidic microenvironment maintained within them (optimal pH is approximately 4.5–5.0), which is an essential prerequisite for the catalytic activity of acid hydrolases [7,8]. Chloride channel, voltage-sensitive 7 (ClC-7) is a chloride antiporter encoded by *CLCN7*. ClC-7 is synthesized in the endoplasmic reticulum (ER) and subsequently localized to lysosomes, where it serves as a key protein responsible for maintaining lysosomal acidification [9]. Dysfunction of ClC-7 disrupts lysosomal pH homeostasis, inhibits enzymatic activity, impairs autophagy, and leads to the accumulation of pathological proteins, thereby contributing to the pathogenesis of neurodegenerative diseases and disorders of lysosomal storage [10]. Studies have shown that reversing ClC-7-related functional defects can alleviate impairment of lysosomal acidification and thereby improve cognitive dysfunction in Alzheimer's disease [11]. However, whether ClC-7 is involved in fluoride-induced defects of lysosomal acidification and its upstream regulatory mechanisms are not known.

Lysosomes serve as a cellular "digestive center". Lysosomes are precisely regulated by ER-mediated signal transduction, membrane trafficking, and metabolic homeostasis [12]. Previously, we revealed that fluoride disrupts the ER–mitochondria coupling structure, induces endoplasmic reticulum stress (ERS), and activates the glycogen synthase kinase 3β (GSK3β) pathway, thereby impairing neuronal activity [13,14]. Upon ERS, the three core unfolded protein response pathways—PERK, IRE1α, and ATF6—are activated [15]. This action initiates transcriptional programs and upregulates expression of the ER chaperone HSP90B1 markedly [16]. HSP90B1 targets substrate proteins *via* ubiquitination and mediates their degradation through the proteasomal or autophagy–lysosomal pathway [17]. Studies have demonstrated that CIC-1 degradation is mediated by cullin4 ubiquitin ligase, and that inhibition of Heat Shock Protein 90 (HSP90) family enhances the stability of CIC-1 markedly [18]. Hence, HSP90B1 may have a broad role in regulation of the stability of transmembrane proteins. However, whether HSP90B1 regulates the stability of ClC-7 *via* a similar ubiquitination mechanism under fluoride-induced neuronal ERS is not known. Therefore, within the context of ER–lysosome crosstalk, we wished to discover how the ER chaperone HSP90B1 regulates lysosomal acidification *via* ubiquitination-dependent modulation of ClC-7 expression.

Strategies for controlling fluoride-induced neurotoxicity are emerging, yet their applicability is limited [13,19,20]. Actively exploring natural, non-toxic phytochemicals for the prevention and treatment of nerve damage represents a future trend.

Diterpene ginkgolides meglumine injection (DGMI) is enriched with active components such as ginkgolides A, B, C, and bilobalide. DGMI is used widely in the treatment of ischemic brain injury and neurodegenerative diseases [21]. Studies have shown that the Ginkgo biloba extract EGb-761 can inhibit neuroinflammation and oxidative stress, reduce neuronal apoptosis, and thereby alleviate fluoride-induced cognitive impairment [22,23]. Its component ginkgolide B readily crosses the blood−brain barrier, improves cognitive function in mice with Alzheimer's disease, reduces Aβ deposition and neuroinflammation, and regulates brain-derived neurotrophic factor (BDNF) expression [24]. *G. biloba extract* exerts improving effects on various cognitive disorders, but whether DGMI can alleviate cognitive impairment induced by fluorosis is not known.

We investigated the key molecular mechanisms underlying fluorosis-induced cognitive dysfunction and evaluated the intervention effect of DGMI. We wished to provide a theoretical basis for potential targeted therapy against fluorosis-induced cognitive impairment.

## 2. Materials and Methods

### *2.1 Chemicals and Reagents*

Sodium fluoride (100 mg/L) was obtained from Shanghai Aladdin Biochemical Technology (Cat. No. S433801, Shanghai, China). DGMI (5 mg/mL) was purchased from Jiangsu Kanion Pharmaceuticals (National Medicine Permit, No. Z20120024, Lianyungang, Jiangsu, China). GSK3β inhibitor (AR-A014418, Catalog No. HY-10512) and agonist (DT-061, Catalog No. HY-112929) were purchased from MedChemExpress (Monmouth Junction, NJ, USA).

### 2.2 Animal Grouping

Male C57BL/6 mice (8 weeks) were housed in the laboratory animal center of Xuzhou Medical University (Xuzhou, Jiangsu, China). Mice were maintained in a room under a constant temperature (23–25 °C) and a 12-h light/dark cycle. Mice had free access to water and standard chow. Only healthy mice free of macroscopic lesions were enrolled, whereas moribund or diseased animals were excluded. C57BL/6 mice were randomly assigned into three experimental groups (Control, NaF, NaF+DGMI, NaF+Clcn7 OE, NaF+DGMI+Clcn7 KD, n = 8 per group). The random allocation sequence was generated by random number method via SPSS 22.0 (IBM, Armonk, NY, USA) software to avoid grouping bias. Cage placement and testing order were randomized to avoid confounding bias.

Control-group mice received sterile pure water. Mice in the NaF group were given sodium fluoride solution (100 mg/L) as drinking water for 90 consecutive days [25]. Mice in the NaF+DGMI group were given sodium fluoride solution (100 mg/L) as drinking water for 90 consecutive days and, from day 61, they were administered DGMI (0.25 mg/d per 20 g body weight) by gavage for 30 consecutive days.

All animal experiments in this study were reported in accordance with the ARRIVE guidelines 2.0, and the completed ARRIVE checklist is provided in **Supplementary Material**.

### 2.3 Morris Water Maze Test (MWMT)

The morris water maze (MWM) consisted of a circular stainless-steel tank (diameter = 120 cm, height = 50 cm) divided into four quadrants. A transparent escape platform (diameter = 10 cm) was placed at the center of one quadrant, submerged 1 cm below the water surface. Water temperature was maintained at 23 ± 2 °C. Skimmed milk powder was added to render the water opaque, thereby concealing the platform. A camera (EoSens 4CXP; Mikrotron, Unterschleißheim, Germany) equipped with an AM41 CMOS image sensor (Alexima, Pasadena, CA, USA) was mounted above the water maze tank to automatically record swimming trajectory, escape latency, swimming speed, time spent in the target quadrant, and the number of platform crossings.

The experiment comprised three phases: adaptation, place navigation training and spatial probe test. During the adaptation phase, conducted 1 day before training, the platform was removed and mice were allowed to swim freely for 60 s to acclimatize to the water environment. Place navigation training lasted 5 consecutive days with four trials per day. Mice were released from different quadrants in a clockwise rotation. Mice failing to locate the platform within 60 s were guided to the platform to rest for 15 s. Trials were separated by 30 min. After each day of training, mice were dried, kept warm, and returned to their home cages. On day 6, the spatial probe test was conducted with the platform removed. Mice were released from the quadrant opposite the original platform and allowed to swim freely for 60 s. The time spent in the target quadrant (%) and the number of crossings over the original platform location were recorded to assess spatial reference memory.

### 2.4 Euthanasia of Mice

The euthanasia of C57BL/6 mice was done using the carbon dioxide ($CO_2$)-inhalation method recommended by GB/T 39760-2021. A high-pressure $CO_2$ cylinder (purity: ≥99.9%) was connected to an airtight euthanasia chamber (volume: ≥6 L) equipped with a flowmeter. The flow rate was set at 28% of the chamber volume per minute (1.68 L/min for a 6-L chamber). Mice were transferred to the chamber (≥1 L of space per mouse to prevent overcrowding), and the chamber was sealed immediately. $CO_2$ was introduced and timed: mice lost consciousness within 2–3 min, and ventilation was continued until respiratory arrest at 5–6 min. Initial death was confirmed by the absence of breathing, loss of corneal reflex, and mydriasis (pupil diameter ≥2 mm). After maintaining $CO_2$ ventilation for an additional 2 min, cervical dislocation was undertaken as secondary form of euthanasia to ensure irreversible death.

### 2.5 Nissl Staining

Following euthanasia, the brain was removed, fixed in 4% paraformaldehyde (C104190, Shanghai Aladdin Biochemical Technology, Shanghai, China), and embedded in paraffin. Paraffin-embedded hippocampi were sliced into 5 µm-thick sections, which were processed for Nissl staining. After dewaxing and rehydration, the sections were treated with cresyl violet stain for 15–20 min at 37 °C and differentiated in ethanol for 1–3 min. Subsequently, the sections were dehydrated rapidly with anhydrous ethanol, cleared in xylene, mounted with neutral balsam, and examined under a microscope. ImageJ 1.51j8 (National Institutes of Health, Bethesda, MD, USA) was used to count Nissl-positive neurons within predefined hippocampal regions of interest (ROIs). The percentage of Nissl-positive cells was calculated as the ratio of Nissl-positive neurons to the total number of neurons in each selected field.

### 2.6 Cell Line and Culture Conditions

The mouse hippocampal neuronal cell line HT22 was kindly provided by the Neurobiology Laboratory of Xuzhou Medical University. Cells were cultured in Dulbecco's modified Eagle's medium supplemented with 10% fetal bovine serum and 1% penicillin–streptomycin, and maintained in a humidified incubator at 37 °C in an atmosphere of 5% $CO_2$. The culture medium was refreshed every 48 h. When cell confluence reached 70–80%, cells were passaged using 0.25% trypsin-ethylenediamine tetraacetic acid. All cell lines were validated *via* short tandem repeat (STR) profiling, and mycoplasma contamination was not detected according to a polymerase chain reaction (PCR)-based assay.

### 2.7 Immunofluorescence

After blockade, brain tissues or fixed cells were permeabilized with 0.1% Triton X-100 for 30 min. Then, samples were incubated with primary antibodies overnight at 4 °C. Following three washes with phosphate-buffered saline (PBS; 5-min each time), samples were incubated with fluorescence-conjugated secondary antibodies (1:500 dilution) at room temperature for 2 h under light-protected conditions. Subsequently, nuclei were counterstained with 4′,6-diamidino-2-phenylindole (DAPI; 1 µg/mL) for 5 min. Fluorescence images were acquired using an inverted fluorescence microscope at standard excitation/emission wavelengths, and analyzed with ImageJ 1.51j8.

### 2.8 Staining With an Acidic Fluorescent Probe

HT22 cells were seeded on coverslips in a 24-well plate. After reaching ~50% confluence, cells were subjected to experimental treatments. Then, the culture medium was removed, and cells were washed gently with pre-warmed PBS. Subsequently, 500 µL of the OG488 probe working solution was added to each well, followed by incubation in the dark for 30 min at 37 °C. After incubation, the dye solution was removed, and cells were washed thrice with PBS. Nuclei were counterstained with DAPI in the dark at room temperature. Coverslips were mounted with anti-fade mounting medium. Lysosomal green fluorescence signals were visualized and images were acquired using an inverted fluorescence or confocal microscope equipped with an excitation filter (488 nm) for quantitative analyses.

### 2.9 Western Blotting

Total proteins were extracted from HT22 cells and hippocampal tissues using radioimmunoprecipitation assay (RIPA) lysis buffer (P0013B; Beyotime Institute of Biotechnology, Shanghai, China) and quantified by the bicinchoninic acid (BCA) method (P0010; Beyotime Institute of Biotechnology). Proteins were separated by sodium dodecyl sulfate-polyacrylamide gel electrophoresis (SDS-PAGE; 10–15% gels, depending on molecular weight) and transferred onto polyvinylidene fluoride (PVDF) membranes. After blockade with 5% skimmed milk, the PVDF membranes were incubated with primary antibodies (detailed in Table 1) overnight at 4 °C, followed by incubation with the appropriate secondary antibody for 2 h at room temperature. Then, the PVDF membranes were washed thrice with Tris-buffered saline with Tween 20 (8 min each time). Protein bands were visualized using enhanced chemiluminescence and captured with a gel-imaging system (Tanon-1600; Shanghai Tanon Science & Technology, Shanghai, China). Band intensities were quantified using ImageJ 1.51j8, and relative protein expression was normalized with respect to β-actin expression.

### 2.10 Co-Immunoprecipitation (Co-IP)

Total cellular proteins were extracted using NP-40 lysis buffer and quantified by the BCA assay. Equal amounts of protein (adjusted to 500 µL with NP-40 buffer) were incubated with the corresponding antibodies according to manufacturer instructions, with immunoglobulin-G as the negative control. The mixtures were rotated overnight at 4 °C. The following day, 40 µL of pre-washed magnetic beads was added to each sample and incubated for 4 h with rotation at 4 °C. Then, the magnetic beads were collected using a magnetic stand and washed thrice with PBS and Tween 20. Finally, 1× SDS loading buffer was added, and samples were boiled for protein denaturation. The resulting samples were stored at −20 °C for short-term use or at −80 °C for long-term storage, pending subsequent SDS-PAGE.

### 2.11 Cell-Viability Assay

Cell viability was assessed using the Cell Counting Kit (CCK)-8 assay. HT22 cells were seeded in 96-well plates and cultured for 24 h. To establish a model of optimal injury, cells were first exposed to NaF (250–2000 µmol/L). Following the establishment of NaF-induced injury at the selected concentration, cells were treated with DGMI (2.5–50 µg/mL). Each group consisted of six replicate wells. After 24 h of treatment, 10 µL of CCK-8 reagent was added to each well followed by incubation for 1 h. The optical density (OD) was measured at 450 nm using a microplate reader. Cell viability (%) was calculated as $[(OD_{experiment} - OD_{blank}) / (OD_{control} - OD_{blank})] \times 100\%$. Data were analyzed and visualized using Prism 8.0.2 (GraphPad, La Jolla, CA, USA) to evaluate the protective effects of DGMI against NaF-induced cytotoxicity.

### 2.12 Apoptosis Assay

Apoptosis was measured using an Annexin V-fluorescein isothiocyanate (FITC)/propidium iodide (PI) apoptosis detection kit (C1062M, Beyotime Biotechnology, Shanghai, China). Briefly, HT22 cells were harvested by trypsinization without ethylenediamine tetraacetic acid. After washing with pre-cooled PBS, cells were resuspended in 500 µL of 1× Annexin V binding buffer. Then, 5 µL of Annexin V-FITC and 5 µL of PI were added to the cell suspension. The mixture was vortex-mixed gently and incubated for 15 min in the dark at room temperature. Stained cells were immediately analyzed by flow cytometry. The green fluorescence of Annexin V-FITC was detected in the FL1 channel at an emission wavelength of 530 nm. The red fluorescence of PI was collected through the FL3 channel at 620 nm.

### 2.13 TUNEL Staining

TUNEL assay in HT22 cells followed a specific design, Cells were washed with pre-cooled PBS and fixed with 4% paraformaldehyde for 25 min at 4 °C. After washing with PBS, samples were permeabilized with 0.2% Tri-

**Table 1. The specific information about the primary antibodies.**

| Antibody | Catalog no. | Dilution | Company | City/Province/Country |
|---|---|---|---|---|
| HSP90B1 | FNab03663 | 1:1000 | FineTest | Wuhan/Hubei/China |
| ClC-7 | AWA63943 | 1:1000 | Affinity Biosciences | Cincinnati/OH/USA |
| p-GSK3β (Tyr216) | ET1607-70 | 1:1000 | Hangzhou Huaan Biotechnology | Hangzhou/Zhejiang/China |
| GSK3β | ET1607-71 | 1:1000 | Hangzhou Huaan Biotechnology | Hangzhou/Zhejiang/China |
| p-mTOR | A5D5 | 1:1000 | Hangzhou Huaan Biotechnology | Hangzhou/Zhejiang/China |
| mTOR | ET1608-5 | 1:1000 | Hangzhou Huaan Biotechnology | Hangzhou/Zhejiang/China |
| PERK | P0074 | 1:1000 | Sigma-Aldrich | Shanghai/China |
| ATF6 | EM1701-94 | 1:1000 | Hangzhou Huaan Biotechnology | Hangzhou/Zhejiang/China |
| IRE1α | A21697 | 1:1000 | Abclonal | Wuhan/Hubei/China |
| TNF-α | DF6440 | 1:1000 | Affinity Biosciences | Cincinnati/OH/USA |
| S100β | A19108 | 1:1000 | Abclonal | Wuhan/Hubei/China |
| IL-6 | WL02841 | 1:1000 | Wanlei Biotechnology | Shenyang/Liaoning/China |
| β-actin | EM21002 | 1:40,000 | Hangzhou Huaan Biotechnology | Hangzhou/Zhejiang/China |

ClC-7, chloride channel, voltage-sensitive 7; GSK3β, glycogen synthase kinase 3β; mTOR, mammalian target of rapamycin; TNF-α, tumor necrosis factor-alpha; IL-6, interleukin-6; HSP90B1, heat shock protein 90 kDa beta member 1; PERK, protein kinase R-like endoplasmic reticulum kinase; ATF6, activating transcription factor 6; IRE1α, inositol-requiring enzyme 1α.

ton X-100 for 5 min at room temperature. Following treatment with equilibration buffer for 10–30 min, the TdT enzyme and Cy5-dUTP labeling mix was added, followed by incubation for 60 min in the dark at 37 °C. After washing with PBS, nuclei were counterstained with DAPI for 5 min protected from light. Slides were mounted with anti-fade mounting medium and examined under a fluorescence microscope. Cy5-red fluorescence (TRITC channel) indicated apoptotic cells, whereas DAPI-blue staining identified all nuclei.

TUNEL staining in the mouse hippocampal sections followed a specific design. Frozen sections of mouse hippocampus were thawed, air-dried, and washed with PBS. Following fixation with 4% paraformaldehyde for 20 min and subsequent washes with PBS, sections were treated with proteinase K (DNase-free; 20 µg/mL) for 30 min at 37 °C. After an additional wash with PBS, freshly prepared TUNEL reaction mixture (TdT enzyme: fluorescent labeling solution = 1:9) was applied, and the sections were incubated in the dark for 30–60 min at 37 °C. Following a final wash with PBS, the sections were mounted with anti-fade mounting medium containing DAPI and scanned using a digital slide scanner (Pannoramic MIDI; 3DHISTECH, Budapest, Hungary). Cell nuclei (blue) and apoptotic cells (red) were visualized by DAPI and TUNEL staining, respectively. Quantitative analyses of TUNEL-positive cells were done using ImageJ 1.51j8.

### *2.14 Plasmid Construction for Gene Overexpression (OE)*

Using mouse cDNA as a template, *Clcn7* and *Marchf1* were amplified by PCR. The primers included protective bases, restriction enzyme sites, and Kozak sequences. The PCR amplification protocol was: 95 °C for 10 min; 35 cycles of 95 °C for 15 s, 65 °C for 15 s, and 72 °C for 3 min; final extension at 72 °C for 5 min. PCR products and the pcDNA3.1(+) vector were digested with the appropriate restriction enzymes. The target DNA fragments were gel-purified and recovered. Ligation was done using T4 DNA ligase with an insert: vector molar ratio of 2:1. The ligation products were transformed into DH5α-competent cells *via* heat shock. Positive clones were selected and confirmed by DNA sequencing.

### *2.15 Construction of Clcn7 Mutant Plasmids*

Site-directed mutagenesis was conducted to generate K86R and K272R mutations into *Clcn7* using BeyoFusion™ polymerase. After PCR amplification, the template plasmid was digested with DpnI. The mutation-containing product was transformed into DH5α-competent cells, and positive clones were screened. Introduction of mutations was confirmed by DNA sequencing.

### *2.16 Construction of Short Hairpin Ribonucleic Acid (shRNA) Knockdown (KD) Plasmids*

The pLKO.1-puro vector was linearized by double digestion with AgeI and EcoRI. Synthetic shRNA oligonucleotides were annealed and subsequently ligated into the linearized backbone. The ligation products were transformed into *Escherichia coli* DH5α-competent cells. Positive clones were selected using Ampicillin resistance followed by verification using Sanger sequencing.

### *2.17 Lentiviral Packaging and Cell Infection*

For lentivirus production, 293T cells were co-transfected with the packaging plasmid pSPAX2, envelope plasmid pMD2.G, and pLKO.1-shRNA transfer vector at a mass ratio of 3:1:4 using lipofection methods. Viral supernatants were collected at 24 h, 48 h and 96 h post-

transfection, and filtered through a 0.45-µm membrane. Target cells were infected with viral supernatant supplemented with polybrene (6 µg/mL) to enhance transduction efficiency. At 48 h post-infection, stable KD cell lines were established by selection with puromycin (1–2 µg/mL). KD efficiency was evaluated by quantitative real-time PCR and/or western blotting. Cell lines were validated via STR profiling, and mycoplasma contamination was not detected according to a PCR-based assay. 293T cells were provided by the Neurobiology Laboratory of Xuzhou Medical University.

*2.18 Stereotaxic Viral Injection Into Mouse Hippocampus*

C57BL/6 mice (8 weeks) were anesthetized using sodium pentobarbital (45 mg/kg, i.p.) and secured in a stereotaxic apparatus (68507, RWD Life Science, Shenzhen, Guangdong, China). Following aseptic preparation, the scalp was incised mid-sagittal to expose the skull. A small burr hole was drilled above the target region. Stereotaxic coordinates were determined relative to the bregma according to *The Mouse Brain in Stereotaxic Coordinates*: dentate gyrus (DG), anteroposterior (AP) −1.96 mm, mediolateral (ML) ±1.50 mm, dorsoventral (DV) −1.70 mm; CA1 region, AP −1.96 mm, ML ±1.50 mm, DV −1.20 mm. The following adeno-associated viral (AAV) vectors (Wuhan Shumi Brain Science Technology, Wuhan, Hubei, China) were injected using a microinjection pump: AAV–CaMKIIa–EGFP (control), AAV-CaMKIIa-*Clcn7*-EGFP-WPRE-hGH polyA (*Clcn7* OE), and AAV-CaMKIIa-*Clcn7*-miR-30-shRNAmir-EGFP-WPRE-hGH polyA (*Clcn7* KD). A volume of 1.0 µL was injected per region at a flow rate of 0.2 µL/min. The needle remained *in situ* for 5 min post-injection before slow withdrawal. The incision was sutured and disinfected subsequently. Mice were placed on a heated pad until full recovery from anesthesia and returned to their home cages.

*2.19 Golgi-Cox Staining*

Freshly dissected whole brains were immersed immediately in Golgi-Cox solution (PK401, FD NeuroTechnologies, Maryland, MD, USA) in amber glass vials, with the solution volume at least 5–10-times the tissue volume. Samples were kept at 20–25 °C on a slow shaker and incubated in the dark for 14 days, with the solution replaced once at day 7. After impregnation, tissues were transferred to 30% sucrose in 0.1 M PBS and stored for 24–72 h at 4 °C until fully submerged. Brains were blotted dry and sectioned in the coronal plane at 100 µm using a vibrating microtome while maintaining PBS moisture and light protection throughout. Intact sections were mounted onto 1% gelatin-coated slides and air-dried for 24–48 h. Development was done according to the manufacturer's protocol, followed by dehydration using a graded series of ethanol solutions, xylene clearing, and DPX mounting. All procedures were protected from light. Waste solutions containing heavy metals or organic solvents were disposed of separately according to regulations relating to hazardous waste.

*2.20 Transmission Electron Microscopy (TEM)*

Mice were deeply anesthetized and perfused in the transcardial region with 0.9% saline followed by fixative containing 4% paraformaldehyde and 2.5% glutaraldehyde in sodium cacodylate buffer (0.1 M, pH 7.4). Brains were dissected and post-fixed in the same fixative for 12 h at 4 °C. Coronal sections (200 µm) were prepared using a vibrating microtome, and tissue blocks (~1 $mm^3$) from the hippocampal CA1 region were excised. Blocks were rinsed in 0.1 M cacodylate buffer, post-fixed in 1% osmium tetroxide for 1 h, washed, and dehydrated through a graded series of ethanol solutions (50%, 70%, 90%, 100%) and acetone. Samples were infiltrated with Epon-812 epoxy resin and polymerized for 48 h at 60 °C. Ultrathin (70 nm) sections were cut using an ultramicrotome, mounted on copper grids, and contrasted with uranyl acetate and lead citrate. Images were acquired using a transmission electron microscope (Tecnai G2 Spirit Twin; FEI, Hillsboro, OR, USA) at 80 kV. Synapses were identified by the presence of presynaptic vesicles, a synaptic cleft, and postsynaptic density (PSD). PSD thickness, length of the active zone, and the density of synaptic vesicles were quantified using ImageJ 1.51j8. After calibrating the scale with ImageJ, the length of synaptic active zones and PSDs were quantified, followed by statistical analyses.

*2.21 Sholl Analyses*

Dendritic complexity was quantified from reconstructed Golgi-stained neurons using ImageJ with the "Sholl Analysis" plugin. The "soma center" was defined as the origin, and concentric circles were applied with a starting radius of 5 µm and 10-µm intervals extending outwards. The plugin automatically counted dendritic intersections at each radius to generate "Sholl profiles". The total number of intersections, maximum number of intersections, and critical radius (radius at maximum intersections) were extracted for statistical analyses. Only neurons with intact soma and complete dendritic arbors were included. Identical analysis parameters were applied across all experimental groups to ensure comparability.

*2.22 Statistical Analyses*

Animals grouping/administration operators and experiment/statistics analysts were blinded to group assignment throughout the study. Statistical analyses were done using SPSS 22.0 (IBM, Armonk, NY, USA). Data are the mean ± SEM. Normality and the homogeneity of variance were assessed by the Shapiro–Wilk test and Levene's test, respectively. Two-group comparisons were made by the Student's *t*-test. Comparisons among multiple groups were evaluated by one-way analysis of variance (ANOVA), followed by *post hoc* analysis with Tukey's multiple com-

parisons test (equal variances assumed) or Dunnett's T3 test (equal variances not assumed). Numbers of biological replicates are specified in each figure legend. Significance was set at $p < 0.05$.

## 3. Results

### *3.1 DGMI Enhances the Percent Survival of Fluoride-Damaged Hippocampal Neurons and Inhibits Neuronal Apoptosis*

To investigate the cytotoxicity of NaF on HT22 cells, the latter were treated with NaF (0, 250, 500, 1000, or 2000 μmol/L) for 24 h. The CCK-8 assay showed that cell viability decreased in a dose-dependent manner at concentrations ≥1000 μmol/L, with a significant reduction in percent survival observed in the 2000 μmol/L group ($p < 0.0001$) (Fig. 1A). Survival at this concentration was ~50%, which induced stable damage while remaining suitable for subsequent observations. Hence, treatment with NaF at 2000 μmol/L for 24 h was selected as the modeling condition.

To evaluate the protective effect of DGMI, HT22 cells were treated with NaF (2000 μmol/L) in combination with DGMI (2.5, 5, 10, 25, or 50 μg/mL) for 24 h. The CCK-8 assay demonstrated that DGMI at 50 μg/mL increased cell viability significantly ($p < 0.0001$) (Fig. 1B), showing the best protective effect. Therefore, this concentration was chosen for subsequent experiments.

Using drug concentrations of 2000 μmol/L for NaF and 50 μg/mL for DGMI, three cell models were established: control, NaF, and NaF+DGMI. TUNEL staining revealed the percentage of apoptotic neurons in the NaF group to be increased significantly compared with that in the control group ($p < 0.0001$), whereas it was reduced markedly in the NaF+DGMI group ($p < 0.001$) (Fig. 1C,D). Furthermore, flow cytometry confirmed these results. The proportion of early apoptotic cells and late apoptotic cells in the control, NaF, and NaF+DGMI groups was 1.27% ± 0.56%, 50.98% ± 3.49%, and 17.82% ± 2.03%, respectively (Fig. 1E,F), further demonstrating that DGMI enhanced the percent survival of NaF-damaged HT22 neurons.

We wished to investigate the protective effect of DGMI on hippocampal neurons in fluoride-exposed C57BL/6 mice. Mouse models were established for the control group, NaF group, and NaF+DGMI group. TUNEL staining revealed that, compared with the control group, the fluorescence quantification in the hippocampus of the NaF group was increased significantly, while DGMI reversed the damage wrought by NaF to neurons (Fig. 2A,B). Nissl staining showed that, compared with the control group, the number of hippocampal neurons in the NaF group was reduced significantly, and cells exhibited shrunken morphology, whereas DGMI alleviated the NaF-induced reduction in neuronal number (Fig. 2C–F). These findings indicated that DGMI inhibited hippocampal neuronal apoptosis and enhanced neuronal survival under NaF intervention.

### *3.2 DGMI Rescues NaF-Induced Synaptic Plasticity Deficits by Alleviating ERS, and Impairment of Lysosomal Acidification*

We employed Golgi staining and TEM to evaluate the regulatory effect of DGMI on hippocampal synaptic plasticity in mice suffering from fluorosis. Golgi staining revealed that NaF exposure reduced dendritic complexity significantly in hippocampal CA1 pyramidal neurons. In contrast, DGMI intervention reversed these structural impairments, leading to a marked increase in the number and branching of dendrites (Fig. 3A,B). Ultrastructural analyses confirmed that the NaF group exhibited significant decreases in synaptic active-zone length and PSD thickness. Notably, DGMI treatment ameliorated these pathologic changes significantly, restoring synaptic active-zone length and PSD thickness (Fig. 3C–E). In conclusion, DGMI alleviated NaF-induced impairments in dendritic structure and synaptic ultrastructure, thereby exerting a protective effect on hippocampal synaptic plasticity.

To ascertain if NaF induces ERS and the interventional role of DGMI, western blotting was done to measure expression of ERS-related proteins (PERK, IRE1α, ATF6). NaF increased the expression of PERK, IRE1α and ATF6 significantly, whereas DGMI reduced their expression markedly (Fig. 4A–D, the original Western blot images are available in the **Supplementary Material-S1**), indicating that DGMI alleviated NaF-induced ERS.

We wished to ascertain if NaF affects lysosomal acidification function and to evaluate the regulatory role of DGMI in this process. We carried out co-localization analysis of lysosomal acidity in HT22 neurons using the acidophilic fluorescent probe OG488 in combination with the lysosomal marker protein LAMP1 (Fig. 4E–H). The intracellular acidic fluorescence intensity was significantly weakened after NaF treatment, suggesting that it induced impairment of lysosomal acidification. Quantitative analysis revealed that NaF markedly reduced the percentage of OG488-positive area colocalized with LAMP1-positive lysosomes, indicating impaired lysosomal acidification under fluoride exposure. In contrast, DGMI intervention partially restored the acidic fluorescence signal, indicating that DGMI could improve the lysosomal acidic environment (Fig. 4I).

### *3.3 DGMI Suppresses GSK3β Expression and Reduces the Expression of the ER Protein HSP90B1 in Hippocampal Neurons*

We wished to investigate if NaF upregulates expression of the ERS marker HSP90B1 by upregulating the expression of GSK3β and to validate the interventional role of DGMI. We added a GSK3β inhibitor (AR-A014418) group and an indirect positive modulator of GSK3β kinase activity (DT-061) group alongside control, NaF, and NaF+DGMI groups. C57BL/6 mice received AR-A014418 (5 mg/kg, i.p., 5 days) or DT-061 (20 mg/kg, i.p., 3 days). West-

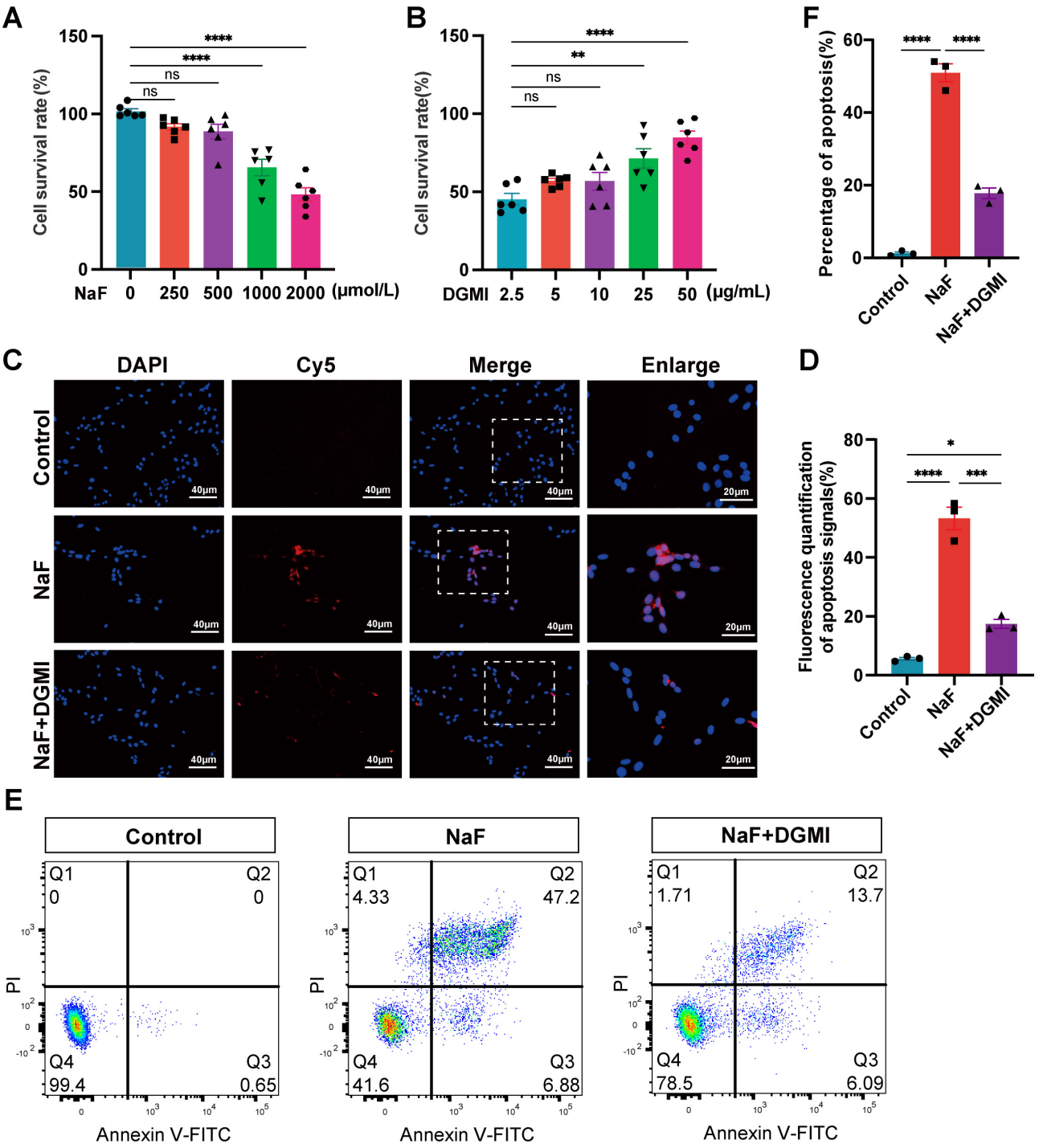


**Fig. 1. DGMI enhances the survival rate of NaF-impaired HT22 neurons and reduces apoptosis**. (A) CCK-8 assay was used to detect cell viability of different concentrations of NaF treatment in HT22 (n = 6). (B) CCK-8 assay was used to detect cell viability of different concentrations of DGMI treatment in HT22 (n = 6). (C,D) Apoptosis in HT22 was detected by TUNEL assay (n = 3), scale bar = 40 μm/20 μm. (E,F) Flow cytometry was employed to detect the apoptosis rate of HT22. The Q2+Q3 quadrants represent apoptotic cells (n = 3). One-way ANOVA was used to evaluate differences among multiple groups, with Tukey's multiple comparisons test applied for *post hoc* pairwise comparisons. The data are presented as the mean ± SEM (*$p < 0.05$, **$p < 0.01$, ***$p < 0.001$, ****$p < 0.0001$, ns indicates no statistical difference). DGMI, diterpene ginkgolides meglumine injection; DAPI, 4′,6-diamidino-2-phenylindole; PI, propidium iodide; FITC, fluorescein isothiocyanate; CCK-8, Cell Counting Kit-8; TUNEL, terminal deoxynucleotidyl transferase dUTP nick-end labeling; ANOVA, analysis of variance.

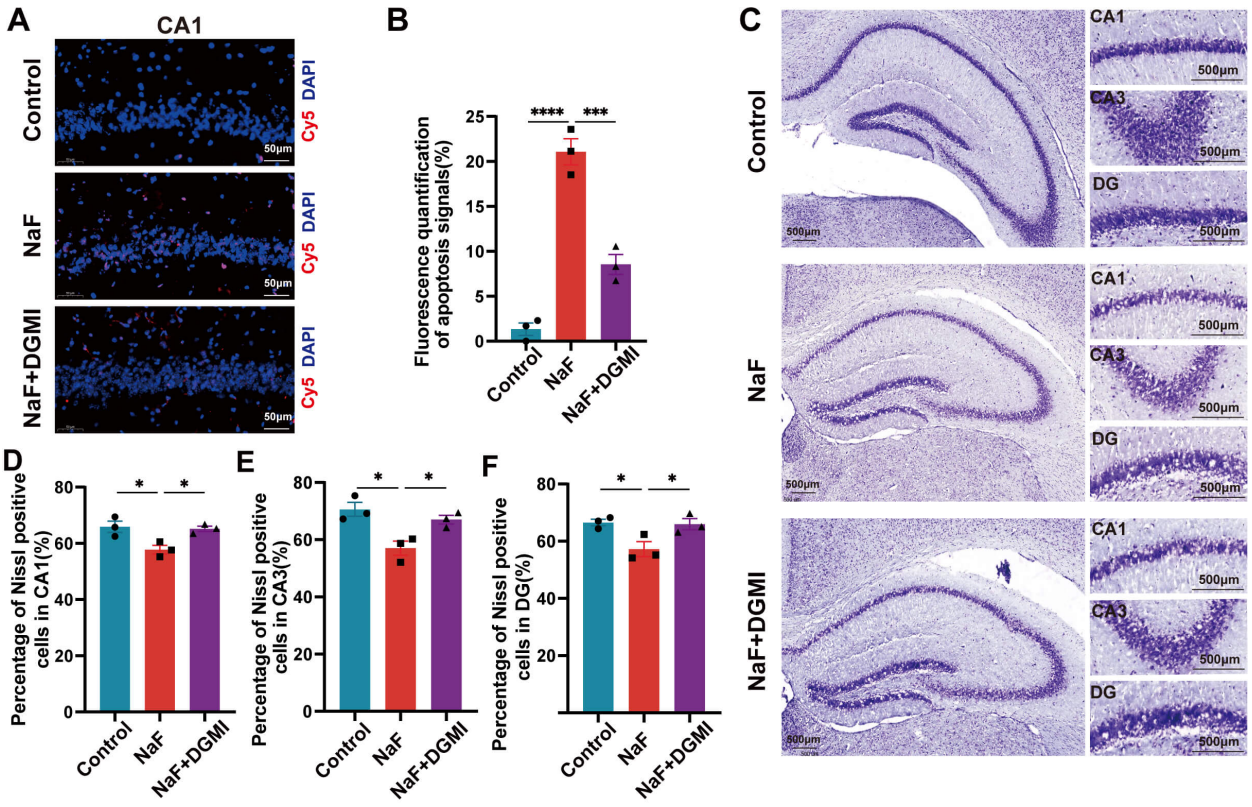


**Fig. 2. DGMI enhances the survival rate and alleviates apoptosis of hippocampal neurons in fluoride-exposed mice**. (A) Neuronal apoptosis in the hippocampal CA1 region of mice in each group detected by TUNEL staining (n = 3), scale bar = 50 μm. (B) Statistical analysis of the immunofluorescence data in figure A. (C) Neuronal survival in the hippocampal CA1, CA3 and DG region of mice in each group by Nissl staining (n = 3), scale bar = 500 μm. (D–F) Cell counting analysis in figure C. One-way ANOVA was used to evaluate differences among multiple groups, with Tukey's multiple comparisons test applied for *post hoc* pairwise comparisons. The data are presented as the mean ± SEM (*$p < 0.05$, ***$p < 0.001$, ****$p < 0.0001$). CA, cornu ammonis; DG, dentate gyrus.

ern blotting of hippocampal tissues (Fig. 5A–C, the original Western blot images are available in the **Supplementary Material-S1**) showed that, compared with the control group, NaF increased protein expression of GSK3β and HSP90B1. The NaF+DGMI group and NaF+AR-A014418 group reduced these levels significantly versus the NaF group, suggesting that GSK3β activity regulated HSP90B1 expression. The NaF+DGMI+DT-061 group showed higher expression of GSK3β and HSP90B1 than the NaF+DGMI group, indicating that DGMI likely suppresses HSP90B1 by modulating GSK3β activity.

In *in vitro* experiments, western blotting was done to measure the expression changes of phosphorylated (p)-mTOR, mTOR, HSP90B1, p-GSK3β, and GSK3β proteins under different treatments (Fig. 5D, the original Western blot images are available in the **Supplementary Material-S1**). Compared with the control group, NaF treatment upregulated the protein expression of p-mTOR, mTOR, HSP90B1, p-GSK3β, and GSK3β significantly. Compared with the NaF group, intervention with NaF+DGMI suppressed the expression of these proteins significantly (Fig. 5E–I).

Co-localization of HSP90B1 protein with the ER in HT22 neurons was also observed by immunofluorescence staining (Fig. 5J,K). The ER marker protein disulfide isomerase (PDI) was shown in green fluorescence while HSP90B1 was in red. Compared with the control group, co-localization of HSP90B1 with PDI in the NaF group was increased significantly. DGMI reversed this effect significantly compared with that in the NaF group.

### *3.4 DGMI Inhibits Formation of the HSP90B1-ClC-7 Complex in Fluoride-Injured HT22 Cells and HSP90B1 Is a Regulator of the Ubiquitination and Degradation of ClC-7*

We carried out Co-IP assays to investigate whether DGMI affects the HSP90B1-ClC-7 interaction by modulating HSP90B1. NaF significantly increased the content of ClC-7 protein that was bound to HSP90B1 or the level of HSP90B1 protein that was bound to ClC-7, compared with that in the control group (Fig. 6A–C, the original Western blot images are available in the **Supplementary Material-S2**), and this effect was reversed by DGMI intervention. The level of interaction in the *Hsp90b1* KD group was comparable with that in the DGMI group, suggesting that DGMI

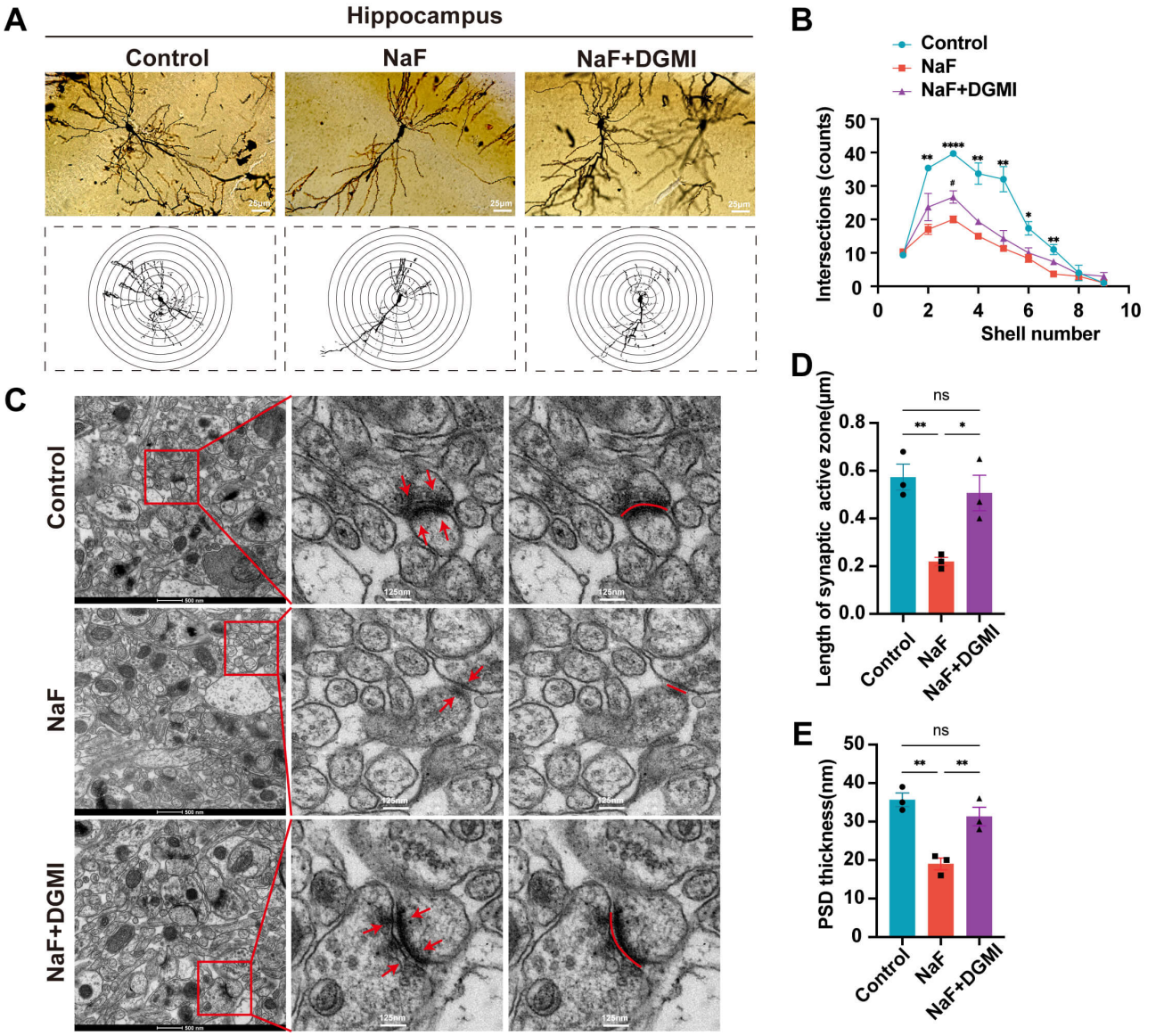


**Fig. 3. DGMI rescues NaF-induced synaptic plasticity deficits in hippocampal neurons**. (A) Golgi staining and Sholl reconstruction analysis of hippocampal CA1 neurons in each group of mice, scale bar = 25 μm. (B) Statistical analysis of the number of dendritic intersections at different radii from the center point via Sholl analysis in each group of mice (n = 3, * Control vs NaF, #NaF vs NaF+DGMI). (C) Electron microscopy images of the hippocampal CA1 region in each group of mice. The length of red curved route indicates synaptic active zone length and the red arrow points to the synaptic membrane at the junction, scale bar = 500 nm, enlarged scale bar = 125 nm. (D,E) Statistical results of the synaptic active zone length (n = 3) and PSD in each group of mice (n = 3). One-way ANOVA was used to evaluate differences among multiple groups, with Tukey's multiple comparisons test applied for *post hoc* pairwise comparisons. The data are presented as the mean ± SEM (*$p < 0.05$, **$p < 0.01$, ****$p < 0.0001$, #$p < 0.05$, ns indicates no statistical difference). PSD, postsynaptic density.

likely regulates the binding by downregulating HSP90B1 expression. These results indicated that NaF promoted formation of the HSP90B1-ClC-7 complex by upregulating HSP90B1 expression, whereas DGMI specifically reduced complex formation by inhibiting HSP90B1. The *Hsp90b1* KD experiment further verified the HSP90B1-dependent nature of the mechanism of action of DGMI.

To investigate the mechanism of ClC-7 ubiquitination, we undertook bioinformatics analysis. Structural alignment revealed that ClC-7 shares a highly similar conformation with CIC-1, including typical transmembrane domains and two cytosolic C-terminal CBS domains (Fig. 6D). Prediction of its potential E3 ubiquitin ligase using Ubibrowser (http://ubibrowser.ncpsb.org.cn) showed that membrane-associated RING-CH protein 1 (MARCHF1) had the highest confidence score (0.865), suggesting it may be the E3 ligase for ClC-7 (Fig. 6E and Table 2).

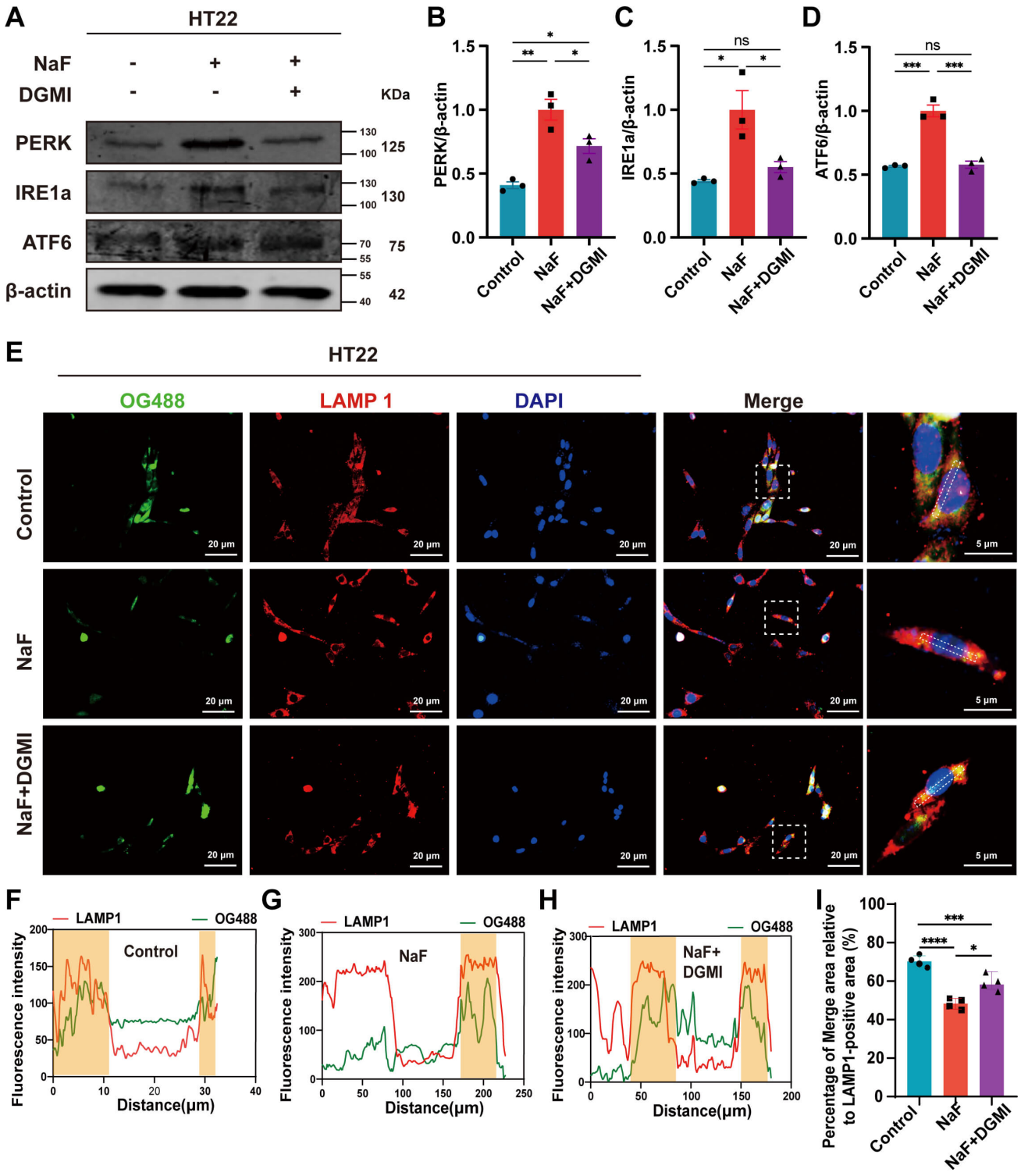


**Fig. 4. DGMI alleviates NaF-induced ERS and lysosomal acidification impairment**. (A) Detection of PERK, IRE1α, ATF6 protein expression in HT22 cells from each group by Western blot (n = 3). (B–D) Statistical analysis of the protein band in figure A. (E) Lysosomal acidity in HT22 cells was detected using an acidotropic pH-sensitive fluorescent probe, scale bar = 20 μm/5 μm (n = 4). (F–H) Fluorescence intensity analysis was performed using OG488 and LAMP1 (n = 4). (I) Quantitative analysis showing the percentage of OG488-positive area colocalized with LAMP1-positive lysosomes (n = 4). One-way ANOVA was used to evaluate differences among multiple groups, with Tukey's multiple comparisons test applied for *post hoc* pairwise comparisons. The data are presented as the mean ± SEM (*$p < 0.05$, **$p < 0.01$, ***$p < 0.001$, ****$p < 0.0001$, ns indicates no statistical difference). ERS, endoplasmic reticulum stress; OG488, Oregon Green 488; LAMP1, lysosome-associated membrane protein 1.

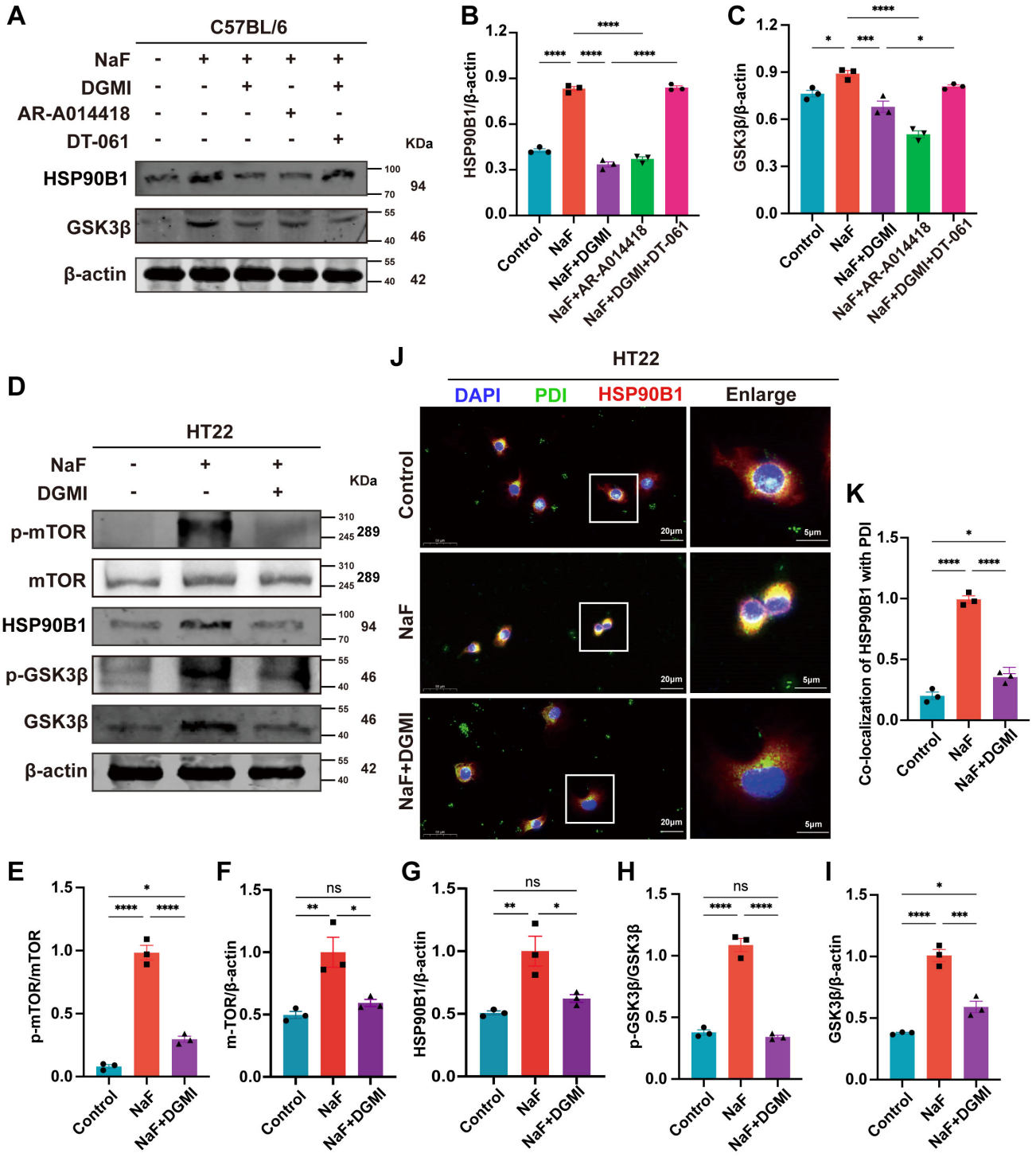


**Fig. 5. DGMI suppresses GSK3β expression and reduces HSP90B1 protein expression on the ER in hippocampal neurons**. (A) Detection of GSK3β and HSP90B1 protein expression levels in the hippocampal tissues of mice from each group by Western blot (n = 3). (B,C) Statistical analysis of the protein band in figure A. (D) Detection of the expression levels of p-mTOR, mTOR, HSP90B1, p-GSK3β, and GSK3β proteins in HT22 cells from each group by Western blot (n = 3). (E–I) Quantification of band intensities in figure D. (J) Representative immunofluorescence images of HSP90B1 (red) and the ER marker PDI (green) co-localization in HT22 neurons from each group, bar = 20 μm/5 μm (n = 3). (K) Quantitative analysis of HSP90B1 protein fluorescence intensity shown in figure J, n = 3. One-way ANOVA was used to evaluate differences among multiple groups, with Tukey's multiple comparisons test applied for *post hoc* pairwise comparisons. The data are presented as the mean ± SEM (*$p < 0.05$, **$p < 0.01$, ***$p < 0.001$, ****$p < 0.0001$, ns indicates no statistical difference). ER, endoplasmic reticulum; PDI, protein disulfide isomerase.

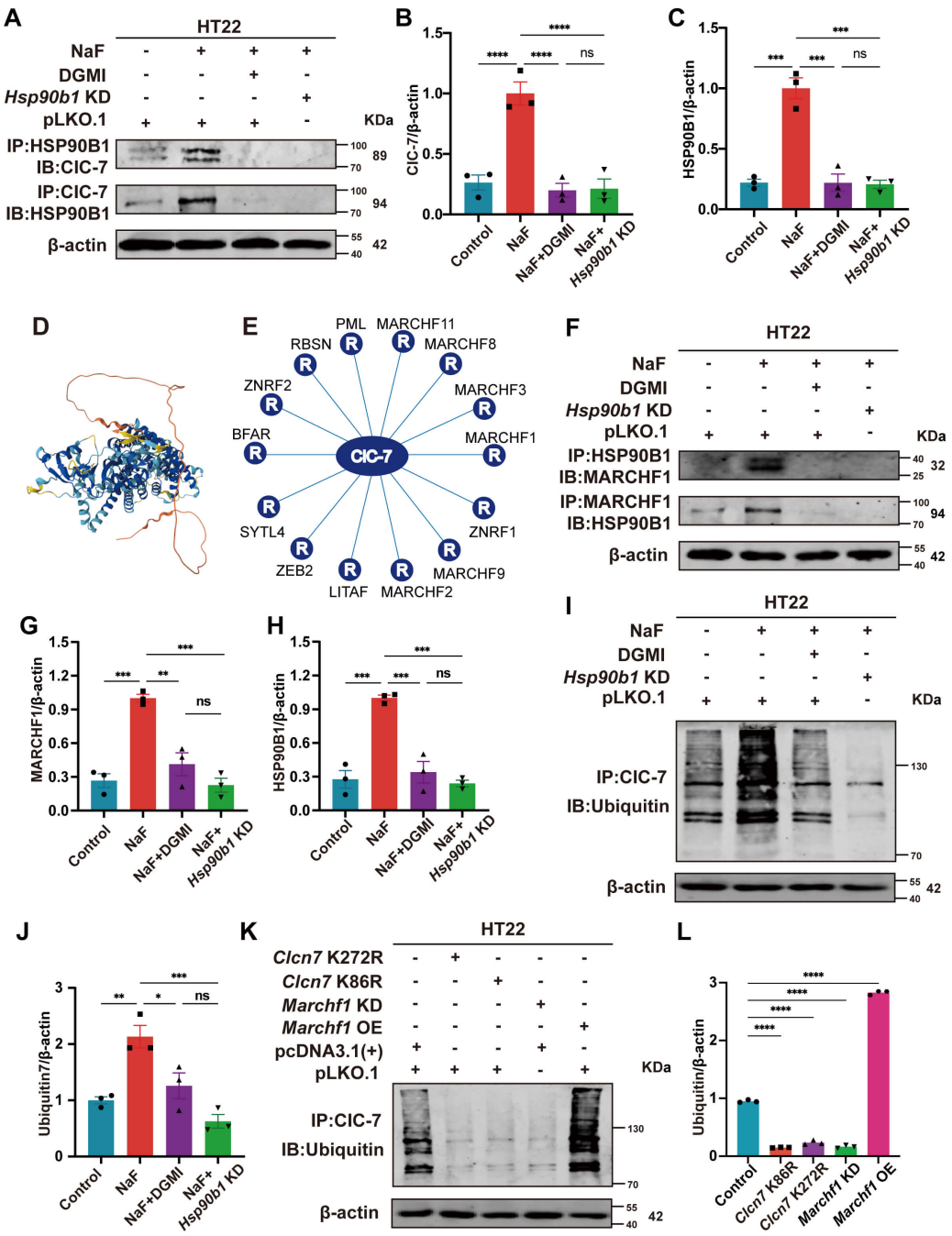


**Fig. 6. DGMI reduces the level of the HSP90B1-ClC-7 complex, and HSP90B1 promotes the ubiquitination of ClC-7 via the E3 ubiquitin ligase MARCHF1**. (A) Detection of ClC-7 and HSP90B1 interaction in HT22 cells by Co-IP. (B,C) Densitometric analysis of bands in figure A (n = 3). (D) Schematic of ClC-7 structure. (E) Prediction of ClC-7's E3 ubiquitin ligase. (F) Interaction between HSP90B1 and MARCHF1 in HT22 cells detected by Co-IP (n = 3). (G,H) Quantitative analysis of band in figure F. (I) Detection of ClC-7 ubiquitination levels by Co-IP (n = 3). (J) Quantitative analysis of bands in figure I (n = 3); (K,L) Grayscale analysis of bands in figure K, n = 3. One-way ANOVA was used to evaluate differences among multiple groups, with Tukey's multiple comparisons test applied for *post hoc* pairwise comparisons. The data are presented as the mean ± SEM (*$p < 0.05$, **$p < 0.01$, ***$p < 0.001$, ****$p < 0.0001$, ns indicates no statistical difference). IP, immunoprecipitation; IB, immunoblotting; OE, overexpression; KD, knockdown.

We carried out Co-IP assays using *Hsp90b1* KD models to determine if HSP90B1 regulates the ubiquitination modification of ClC-7 through interaction with MARCHF1. NaF treatment promoted the binding between HSP90B1 and MARCHF1 (Fig. 6F–H, the original Western blot images are available in the **Supplementary Material-S2**). This promoting effect was markedly blocked following DGMI intervention or *Hsp90b1* KD. Further re-

**Table 2. Prediction of ClC-7's E3 ubiquitin ligase.**

| Protein Symbol(E3) | Protein Symbol(Substrate) | Go_LikelihoodRatio | Confidence Score |
|---|---|---|---|
| MARCHF1 | ClC-7 | 7.74 | 0.865 |
| MARCHF3 | ClC-7 | 5.35 | 0.845 |
| MARCHF8 | ClC-7 | 5.35 | 0.845 |
| MARCHF11 | ClC-7 | 5.35 | 0.845 |
| PML | ClC-7 | 5.35 | 0.845 |
| RBSN | ClC-7 | 5.35 | 0.845 |
| ZNRF2 | ClC-7 | 5.35 | 0.845 |
| BFAR | ClC-7 | 3.63 | 0.821 |
| SYTL4 | ClC-7 | 3.63 | 0.821 |
| ZEB2 | ClC-7 | 3.63 | 0.821 |
| LITAF | ClC-7 | 3.03 | 0.809 |
| MARCHF2 | ClC-7 | 3.03 | 0.809 |
| MARCHF9 | ClC-7 | 3.03 | 0.809 |
| ZNRF1 | ClC-7 | 3.03 | 0.809 |

MARCHF, Membrane-associated RING-CH-type finger protein X; PML, promyelocytic leukemia; RBSN, rabenosyn, RAB effector; ZNRF, zinc and ring finger; BFAR, bifunctional apoptosis regulator; SYTL, synaptotagmin-like; ZEB, zinc-finger E-box-binding homeobox; LITAF, lipopolysaccharide-induced TNF factor.

ciprocal Co-IP assays targeting MARCHF1 verified these findings, yielding highly consistent results, confirming the specificity and reliability of the NaF-induced HSP90B1–MARCHF1 interaction. NaF treatment upregulated ClC-7 ubiquitination significantly (Fig. 6I,J, the original Western blot images are available in the **Supplementary Material-S2**). DGMI intervention and *Hsp90b1* KD reversed this effect significantly, with no significant difference between the two intervention groups. Collectively, these results indicated that the ubiquitination modification of ClC-7 was dependent upon HSP90B1 expression.

To further investigate if MARCHF1 mediates ClC-7 ubiquitination directly, we used UbPred (http://www.ubpred.org/) to predict potential ubiquitination sites on ClC-7. We identified K86 and K272 as high-confidence candidates. Subsequently, we constructed ClC-7 point-mutant plasmids (pcDNA3.1(+)-*Clcn7*-K86R and -K272R) and combined them with *Marchf1* OE or KD plasmids for Co-IP functional validation. K86R and K272R mutations reduced ClC-7 ubiquitination significantly. *Marchf1* KD inhibited ubiquitination markedly, whereas *Marchf1* OE had the opposite effect (Fig. 6K,L, the original Western blot images are available in the **Supplementary Material-S2**). These data confirmed that MARCHF1 was the E3 ubiquitin ligase that regulated ClC-7 ubiquitination by modifying K86 and K272 sites.

### *3.5 DGMI Alleviates Impairment of Lysosomal Acidification by Regulating ClC-7 Expression, Thereby Ameliorating Cognitive Deficits in Mice With Fluorosis*

NaF treatment reduced ClC-7 expression significantly compared with that in the control group, whereas this reduction was rescued markedly by NaF+DGMI and NaF+*Clcn7* OE interventions. Notably, *Clcn7* KD in the context of DGMI treatment led to a significant decrease in ClC-7 expression (Fig. 7A,B, the original Western blot images are available in the **Supplementary Material-S2**). Consistently, NaF decreased ClC-7 localization on the lysosomal membrane significantly relative to that in the control group (Fig. 7C,D). This effect was reversed by NaF+DGMI and NaF+*Clcn7* OE interventions. Importantly, *Clcn7* KD under DGMI treatment reduced its lysosomal localization markedly, demonstrating that DGMI preserved ClC-7 function by increasing the lysosomal localization of ClC-7.

Using the OG488 lysosomal acidotropic probe combined with LAMP1 immunostaining, we analyzed the lysosomal acidification in HT22 cells. Compared with that in the control group, the OG488 fluorescence signal was significantly weakened in neurons after NaF treatment (Fig. 7E,F), indicating marked inhibition of the lysosomal acidic environment. Following DGMI intervention, the acidic fluorescence signal was enhanced significantly compared with that in the NaF group, suggesting a protective effect of DGMI on lysosomal function. Furthermore, under the NaF+*Clcn7* OE condition, lysosomal acidic fluorescence was also significantly stronger than in the NaF group, an effect similar to that of DGMI. However, when ClC-7 expression was knocked down in the NaF+DGMI group, the OG488 fluorescence quantification decreased significantly again, returning to a level close to that of the NaF group. These results indicated that DGMI may alleviate NaF-induced impairment of lysosomal acidification. This protective effect was mimicked by *Clcn7* OE and attenuated significantly by *Clcn7* KD, suggesting that ClC-7 was a key target through which DGMI regulates lysosomal acidification function.

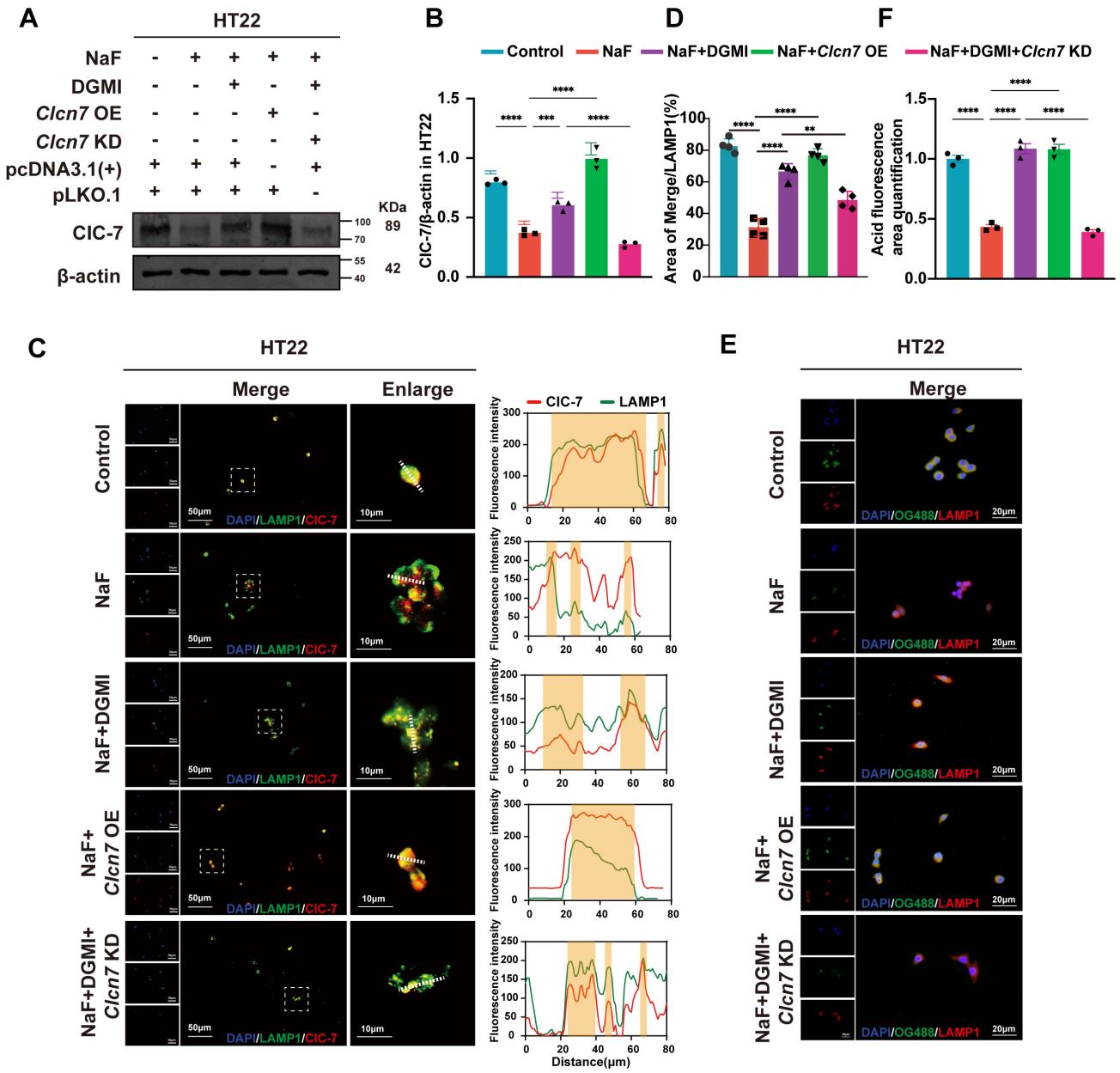


**Fig. 7. DGMI enhances the abundance of ClC-7 on the lysosomal membrane, thereby promoting lysosomal acidification**. (A) Western blot analysis of ClC-7 protein expression in HT22 cells (n = 3). (B) Statistical analysis of band grayscale values in figure A, n = 3. (C) Immunofluorescence representative images showing the co-localization of the lysosomal marker LAMP1 (green) and ClC-7 (red) in HT22 neurons from each treatment group, scale bar = 50 μm/10 μm (n = 4). (D) Co-localization analysis of LAMP1 and ClC-7 in figure C, n = 4. (E) Immunofluorescence detection of OG488 (green) and LAMP1 (red) in HT22 cells from different treatment groups, scale bar = 20 μm (n = 3). (F) Statistical analysis of co-localization of OG488 (green) and LAMP1 (red) in HT22 neurons from each treatment group in figure E, n = 3. One-way ANOVA was used to evaluate differences among multiple groups, with Tukey's multiple comparisons test applied for *post hoc* pairwise comparisons. The data are presented as the mean ± SEM (**$p < 0.01$, ***$p < 0.001$, ****$p < 0.0001$).

We wished to ascertain if DGMI protects cognitive function by regulating ClC-7 expression. We established *Clcn7*-OE and *Clcn7*-KD mouse models, and cognitive function was assessed using the MWMT. Western blotting confirmed model construction (Fig. 8A–D, the original Western blot images are available in the **Supplementary Material-S2**). There were no statistically significant differences in total travel distance, mean swimming speed, maximum swimming speed, and latency to first platform entry in the MWMT among all groups (**Supplementary Material-S3 A–D**). The MWMT (Fig. 8E–G) revealed that mice in the NaF group exhibited significantly fewer platform cross-

ings and shorter time spent in the target quadrant compared with those in the control group, consistent with cognitive impairment. DGMI treatment or *Clcn7* OE reversed these effects, with both indices improved significantly, indicating alleviation of NaF-induced cognitive damage. However, *Clcn7* KD partially abolished the cognitive benefits conferred by NaF+DGMI, reducing platform crossings and target quadrant time to levels close to those in the NaF group. These data indicated that ClC-7 may serve as a key mediator of the neuroprotective effects of DGMI.

## 4. Discussion

Fluorosis is prevalent in "developing" countries. Exposure to excessive amounts of fluoride can lead to cognitive symptoms in children, including reduced intelligence quotient, impaired memory, and compromised attention. Animal models of fluoride-induced cognitive impairment were established in 2001. Among them, the method of constructing cognitive-dysfunction models in C57BL/6 mice *via* administration of drinking water containing sodium fluoride (100 mg/L) has been validated in numerous studies, thereby laying a solid foundation for further elucidating the molecular mechanisms underlying fluoride neurotoxicity [26,27]. These mechanisms are complex and may involve oxidative stress, neuronal apoptosis, neuroinflammation, and deposition of pathologic proteins, but the precise regulatory factors have not been fully elucidated [28]. A study has shown that *G. biloba extract* can ameliorate cognitive dysfunction in rats suffering from fluorosis by inhibiting hippocampal neuronal apoptosis and oxidative-stress injury [23]. However, the molecular mechanism underlying its neuroprotective effect in fluorosis models is incompletely understood. As a marketed drug in China, DGMI has been well validated for safety and toxicology in numerous studies [29,30]. Despite wide clinical use for ischemic cerebrovascular diseases, its efficacy against fluorosis-induced cognitive dysfunction remains unclear. We aimed to systematically investigate the protective effect of DGMI against fluoride-induced hippocampal neuronal damage in HT22 cells and C57BL/6 mice, as well as its underlying molecular mechanism.

The findings from Fig. 1 enabled identification of optimal modeling conditions and drug dose, prompting us to treat HT22 cells with NaF at 2000 μmol/L and DGMI at 50 μg/mL for 24 h in subsequent experiments. Flow cytometry and TUNEL staining collectively demonstrated that NaF exposure induced significant neuronal apoptosis and impaired cell viability, whereas DGMI intervention reversed these pro-apoptotic effects and exerted a robust cytoprotective role. Notably, the anti-apoptotic activity of DGMI upon hippocampal neurons was observed consistently in cellular experiments and the fluorosis model in mice (Fig. 2), underscoring the translational potential of DGMI in mitigating fluoride-induced neurotoxicity.

Numerous studies have established that fluoride-induced neuronal apoptosis is a complex pathologic process orchestrated by multiple signaling pathways and molecular targets, rather than being mediated by a single independent mechanism [14,28,31]. Our findings demonstrated that fluoride exposure downregulated the expression of synaptic structural proteins significantly, impaired PSD integrity, and reduced dendritic spine density and synaptic transmission efficiency, thereby compromising synaptic plasticity processes such as long-term potentiation. Notably, neuronal apoptosis and inhibition of synaptic plasticity are not mutually exclusive; instead, they interact *via* shared signaling pathways to synergistically exacerbate neural damage. On the one hand, excessive apoptosis induces massive neuronal loss, directly undermining the structural basis for synaptogenesis. On the other hand, impaired synaptic plasticity leads to insufficient neurotrophic signaling and aberrant synaptic transmission, which further promotes neuronal apoptosis. Collectively, these results indicated that fluorosis elicited nervous-system impairment through concurrent induction of neuronal apoptosis and synaptic plasticity deficits, targeting cell survival and synaptic function and, ultimately, contributing to cognitive impairment.

Concomitantly, fluoride exposure-induced ERS and impaired lysosomal acidification constitute additional critical pathways mediating neuronal apoptosis. As the central "hub" governing protein folding and calcium homeostasis, the ER is highly vulnerable to fluorosis-elicited dysfunction. Fluoride intoxication aberrantly activates the unfolded protein response (UPR), driving sustained activation of the PERK-eIF2α-ATF4-CHOP signaling cascade, while disrupting calcium-store equilibrium in the ER and thereby triggering intracellular calcium overload. In parallel, compromised lysosomal acidification suppresses the catalytic activity of acid hydrolases, impedes normal progression of autophagic flux, and promotes the accumulation of damaged proteins and organelles, ultimately exacerbating disruption of intracellular homeostasis [32]. Our results confirmed that fluorosis can induce ERS and impaired lysosomal acidification, and that the anti-apoptotic effect of DGMI may be achieved by regulating the functions of the ER and lysosomes. However, as essential functional organelles within a cell, the specific molecular mechanisms underlying the crosstalk between the ER and lysosomes in fluorosis-induced neurological injury are unclear. A study has suggested that calcium overload in the ER may disrupt the stability of lysosomal membranes, and that abnormal function of lysosomal enzymes may, in turn, exacerbate ER damage [33]. Nevertheless, direct experimental evidence is lacking regarding the key signaling molecules involved in this "bidirectional regulation", their upstream–downstream hierarchy, and their synergistic interactions with other mechanisms. Given this critical knowledge gap, we explored the molecular mechanisms underlying the crosstalk between lysosomes and the ER.

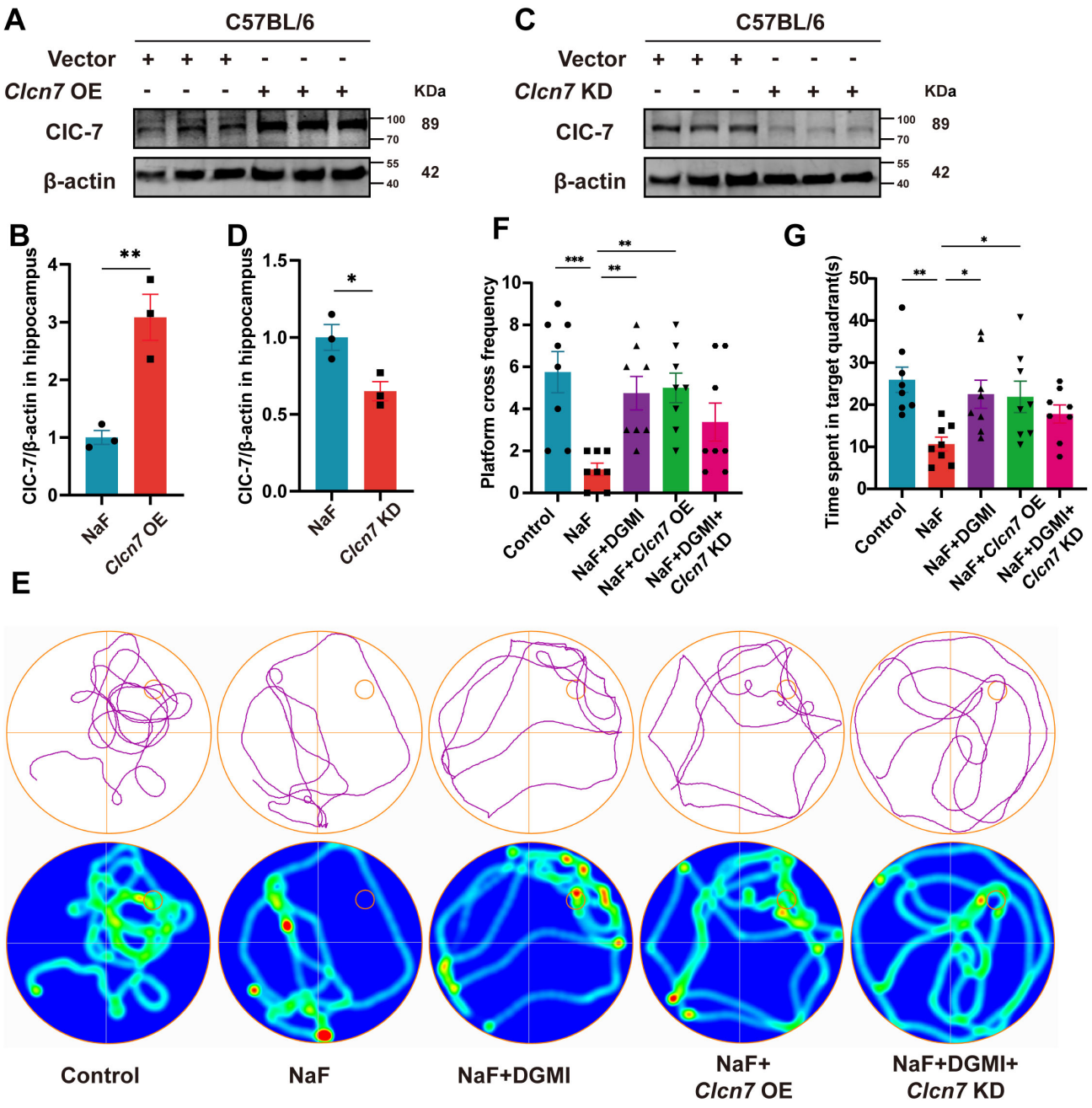


**Fig. 8. DGMI mediates its cognitive protective effect through regulating ClC-7.** (A,B) Western blot validated the efficacy of ClC-7 OE (n = 3). (C,D) Western blot validated the efficacy of ClC-7 KD (n = 3). (E) Representative swimming trajectories of mice from each group in the Morris water maze test. (F,G) Statistical analysis of the platform crossings and time spent in the target quadrant in Morris water maze test (n = 8). One-way ANOVA was used to evaluate differences among multiple groups, with Tukey's multiple comparisons test applied for *post hoc* pairwise comparisons. The data are presented as the mean ± SEM (*$p < 0.05$, **$p < 0.01$, ***$p < 0.001$).

HSP90B1 (also known as endoplasmic reticulum-resident glycoprotein 96) is a key molecule that maintains ER homeostasis and regulates immune–inflammatory responses, with its upregulated expression a hallmark of ERS activation [34]. GSK3β, a constitutively active serine/threonine kinase, serves as a central regulatory node in multiple signaling pathways, including Wnt/β-catenin, nuclear factor kappa-B (NF-κB), phosphoinositide 3-kinase/protein kinase B (PI3K/Akt), and ERS. Dysregulated activation of GSK3β is closely implicated in inflammation, tumorigenesis, and neurodegenerative diseases [35,36]. Our previous work revealed that fluorosis can induce ERS accompanied by significant upregulation of GSK3β expression [14]. Building on this finding, the present study incorporated interventions by a GSK3β agonist and GSK3β inhibitor to validate the positive regulatory

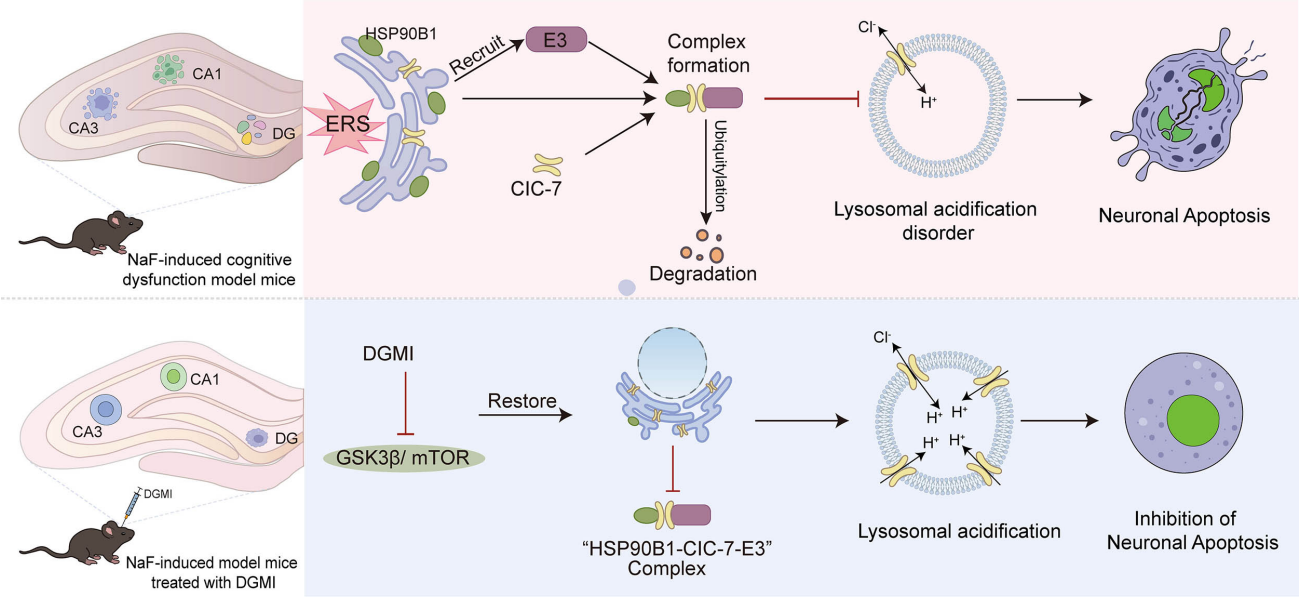


**Fig. 9. Schematic illustration of the underlying mechanism**. Arrows denote facilitative effects, while T-shaped symbols indicate inhibitory effects.

effect of GSK3β upon HSP90B1. Concurrently, investigations into the expression and phosphorylation of mTOR (an upstream regulatory molecule of GSK3β) were done to clarify its mechanistic role in fluorosis-associated ERS pathways. Collectively, our results demonstrated that NaF induced aberrant accumulation of HSP90B1 in the ER and triggered ERS through activation of the mTOR/GSK3β signaling axis. In contrast, DGMI exerted neuroprotective effects by inhibiting the phosphorylation of key molecules in this pathway and attenuating ERS-induced damage.

ClC-7 is synthesized in the ER and targeted to the lysosomal membrane *via* the ER-to-lysosome trafficking pathway. It serves as a key $Cl^-/H^+$ antiporter essential for maintaining lysosomal acidification [11]. Abnormal expression of ClC-7 disrupts lysosomal pH homeostasis, inhibits enzymatic activity, and impairs autophagy. A study has shown that mutations in ClC-7 impair lysosomal acidification and result in defects of lysosomal storage [37]. Furthermore, ClC-7 has been implicated in Alzheimer's disease-related pathology, as microglial degradation of amyloid fibrils requires the delivery of ClC-7 to lysosomes, highlighting the importance of ClC-7-mediated lysosomal function in amyloid clearance [38]. A study on degradation of transmembrane proteins have shown that HSP90B1 regulates the ubiquitination of CIC-1 *via* the Cullin4 E3 ubiquitin ligase, thereby maintaining its protein stability, suggesting that HSP90B1 may serve as an important regulator of ubiquitination [18]. ClC-7 is highly homologous to CIC-1, sharing similar transmembrane domains and a cytoplasmic C-terminus composed of cystathionine-β-synthase domains. However, whether HSP90B1 regulates the ubiquitination and degradation of ClC-7 through a similar mechanism in a fluorosis-induced nerve-injury model is not known. In the present study, Ubibrowser was used to predict potential E3 ubiquitin ligases for ClC-7. We found MARCHF1 to be the most likely E3 ligase catalyzing the ubiquitination of ClC-7. Therefore, we hypothesize that HSP90B1 may promote the ubiquitination and degradation of ClC-7 by recruiting the E3 ligase MARCHF1.

To elucidate the molecular mechanism by which HSP90B1 regulates ClC-7, we undertook HSP90B1 knockdown and protein–protein interaction assays. NaF upregulated HSP90B1 expression, enhancing its binding to ClC-7 and promoting its interaction with MARCHF1, whereas DGMI treatment or HSP90B1 knockdown blocked the formation of these complexes. These data indicated that HSP90B1 acts as an upstream regulator of MARCHF1, mediating the toxic effects of NaF and the protective effects of DGMI. Ubiquitination assays showed that NaF induced ClC-7 ubiquitination, which could be reversed by DGMI or HSP90B1 knockdown. Mutagenesis of ClC-7 ubiquitination sites and manipulation of MARCHF1 expression identified K86 and K272 as the key ubiquitination sites and MARCHF1 as the essential E3 ubiquitin ligase for ClC-7. Collectively, we revealed a novel signaling axis: NaF activates the HSP90B1–MARCHF1 pathway to promote ubiquitination and degradation of ClC-7 at K86 and K272 residues, whereas DGMI targets and inhibits HSP90B1 to block this axis and maintain the stability of ClC-7 protein.

Through overexpression and knockdown of ClC-7, combined with immunofluorescence co-localization and lysosomal acidification probe detection, we further clarified the central role of ClC-7 in the regulation of lysosomal function by DGMI. NaF exposure suppressed the targeted enrichment of ClC-7 to lysosomes markedly, whereas DGMI intervention or direct ClC-7 overexpression restored

this distribution pattern. In contrast, ClC-7 knockdown following NaF+DGMI treatment attenuated the lysosomal localization of ClC-7, suggesting that the regulation of ClC-7 lysosomal enrichment by DGMI is an essential prerequisite for its protective effects. Meanwhile, lysosomal acidification assays confirmed that NaF-induced dysfunction of lysosomal acidification was ameliorated significantly by DGMI or ClC-7 overexpression, whereas ClC-7 KD reversed the protective effects of DGMI and "reimpaired" the lysosomal acidic microenvironment. Collectively, these findings demonstrated that DGMI alleviated fluorosis-induced dysfunction of lysosomal acidification by upregulating ClC-7 expression and promoting its targeted enrichment to lysosomes. The expression and subcellular localization of ClC-7 serve as key nodes in the regulation of lysosomal acidification and represent the core mechanism underlying the neuroprotective effects of DGMI. This discovery further refines the molecular network by which DGMI targets and modulates fluoride-induced neurological injury.

Collectively, these findings demonstrate that DGMI upregulates ClC-7 expression by suppressing ubiquitin-mediated degradation and facilitates its functional localization on the lysosomal membrane, thereby preserving the lysosomal acidic microenvironment. This discovery provides critical experimental evidence for elucidating the neuroprotective mechanism of DGMI against fluoride-induced neurological injury. Furthermore, evaluations using fluorosis mouse models with ClC-7 overexpression or knockdown revealed that NaF-induced significant cognitive impairment was markedly ameliorated by DGMI intervention or ClC-7 overexpression, while ClC-7 knockdown following NaF+DGMI treatment notably reversed this cognitive protection. These results indicate that the ameliorative effect of DGMI on fluorosis-associated cognitive dysfunction is largely dependent on its regulation of ClC-7 expression, with ClC-7 expression and lysosomal localization being modulated by the ubiquitination pathway mediated by the ER chaperone protein HSP90B1.

## 5. Limitations

Our study had four main limitations. First, we established fluorosis models only using mice and cell lines, without verifying the protective effect of DGMI in fluorosis-affected populations or primary neurons. Therefore, the generalizability of its cognitive protective effects still needs to be confirmed in more diverse models. Second, although the sample size meets the requirements for mechanistic studies, it may still limit the generalizability of the results. In future studies, we will increase the sample size and add independent experimental batches to improve data reliability. Third, direct measurement of MARCH1 enzymatic activity is currently not feasible. The available commercial kits require purified protein, which cannot reflect physiological conditions or intergroup differences in the microenvironment, making it difficult to accurately determine the authentic MARCH1 activity in each group. Four, although swimming speed and locomotor parameters were comparable among groups, acquisition training latency and visible-platform trials were not included in the original experimental design, which represents a limitation of the present study.

## 6. Conclusions

It is likely that DGMI downregulates the ER chaperone HSP90B1, attenuates its binding to CIC-7, and thereby may inhibit MARCH1 E3 ligase-dependent ubiquitination and degradation of CIC-7 at K86 and K272. This process might promote the functional distribution of CIC-7 on the lysosomal membrane, rescue lysosomal acidification, and eventually could ameliorate cognitive impairment in mice. Fig. 9 summarizes the molecular mechanism by which the HSP90B1-MARCHF1-ClC-7 axis exerts neuroprotective effects by regulating lysosomal function in the fluorosis model.

## Availability of Data and Materials

The datasets used and analyzed during the current study are available from the corresponding author upon reasonable request.

## Author Contributions

RC and PX were involved in the experimental design, collection and analysis of core data, and drafting of the initial manuscript. XRF and ZHZ carried out experiments and acquired laboratory data. CYM provided technical support for academic issues and contributed to result analysis. QHJ was involved in the experimental design and responsible for revision and polishing of the manuscript, and provided financial support for this study. All authors contributed to editorial changes in the manuscript. All authors read and approved the final version of the manuscript. All authors have participated sufficiently in the work and agreed to be accountable for all aspects of the work.

## Ethics Approval and Consent to Participate

Animal experiments were conducted in accordance with the Guide for the Care and Use of Laboratory Animals (Eighth Edition; US National Institutes of Health, Bethesda, MD, USA) and the ARRIVE guidelines 2.0. The study protocol was approved (SUDA20260206A05) by the animal ethics committee of Soochow University (Suzhou, China).

## Acknowledgment

We sincerely thank our colleagues at Soochow University, Xuzhou Medical University, Nanjing Medical University, and Nantong University, as well as their affiliated hospitals, for their invaluable support. The stimulating academic environment and invaluable resources provided by

these institutions laid the essential foundation for our work. Finally, we express our special gratitude to Yeming Zhou from the Department of Emergency Medicine, The Fourth Affiliated Hospital of Nanjing Medical University, for his technical guidance and valuable suggestions on cell experiments.

## Funding

This work was supported by the Huai'an Natural Science Foundation (HAB202315) and the Jiangsu Provincial Young Science and Technology Talent Support Project (JSTJ-2025-880).

## Conflicts of Interest

The authors declare no conflicts of interest.

## Supplementary Material

Supplementary material associated with this article can be found, in the online version, at https://doi.org/10.31083/JIN53296.

## References

[1] Jha SK, Mishra VK, Sharma DK, Damodaran T. Fluoride in the environment and its metabolism in humans. Reviews of Environmental Contamination and Toxicology. 2011; 211: 121–142. https://doi.org/10.1007/978-1-4419-8011-3_4

[2] Ghosh A, Patra S, Bhattacharjee S, Bera B. Severe magnitude of dental and skeletal fluorosis and its impact on society and environment in a part of Manbhum-Singhbhum Plateau, India. BMC Public Health. 2024; 24: 1971. https://doi.org/10.1186/s12889-024-19446-1

[3] Taylor KW, Eftim SE, Sibrizzi CA, Blain RB, Magnuson K, Hartman PA, et al. Fluoride Exposure and Children's IQ Scores: A Systematic Review and Meta-Analysis. JAMA Pediatrics. 2025; 179: 282–292. https://doi.org/10.1001/jamapediatrics.2024.5542

[4] Liu W, Wang C, Tang H, Tian Z, Li D, Chen G, et al. Mitochondrial translation impairment-triggered neuroinflammation mediates fluoride-induced cognitive deficits. Ecotoxicology and Environmental Safety. 2025; 305: 119187. https://doi.org/10.1016/j.ecoenv.2025.119187

[5] Zhang J, Tang Y, Hu Z, Xu W, Ma Y, Xu P, et al. The inhibition of TRPML1/TFEB leads to lysosomal biogenesis disorder, contributes to developmental fluoride neurotoxicity. Ecotoxicology and Environmental Safety. 2023; 250: 114511. https://doi.org/10.1016/j.ecoenv.2023.114511

[6] Tang H, Hou H, Song L, Tian Z, Liu W, Xia T, et al. The role of mTORC1/TFEB axis mediated lysosomal biogenesis and autophagy impairment in fluoride neurotoxicity and the intervention effects of resveratrol. Journal of Hazardous Materials. 2024; 467: 133634. https://doi.org/10.1016/j.jhazmat.2024.133634

[7] Lübke T, Lobel P, Sleat DE. Proteomics of the lysosome. Biochimica et Biophysica Acta. 2009; 1793: 625–635. https://doi.org/10.1016/j.bbamcr.2008.09.018

[8] Hu M, Chen J, Liu S, Xu H. The Acid Gate in the Lysosome. Autophagy. 2023; 19: 1368–1370. https://doi.org/10.1080/15548627.2022.2125629

[9] Cao X, Lenk GM, Mikusevic V, Mindell JA, Meisler MH. The chloride antiporter CLCN7 is a modifier of lysosome dysfunction in FIG4 and VAC14 mutants. PLoS Genetics. 2023; 19: e1010800. https://doi.org/10.1371/journal.pgen.1010800

[10] Kasper D, Planells-Cases R, Fuhrmann JC, Scheel O, Zeitz O, Ruether K, et al. Loss of the chloride channel ClC-7 leads to lysosomal storage disease and neurodegeneration. The EMBO Journal. 2005; 24: 1079–1091. https://doi.org/10.1038/sj.emboj.7600576

[11] Lee JH, Wolfe DM, Darji S, McBrayer MK, Colacurcio DJ, Kumar A, et al. β2-adrenergic Agonists Rescue Lysosome Acidification and Function in PSEN1 Deficiency by Reversing Defective ER-to-lysosome Delivery of ClC-7. Journal of Molecular Biology. 2020; 432: 2633–2650. https://doi.org/10.1016/j.jmb.2020.02.021

[12] Thakur RS, O'Connor-Giles KM. PDZD8 promotes autophagy at ER-lysosome membrane contact sites to regulate activity-dependent synaptic growth. Cell Reports. 2025; 44: 115483. https://doi.org/10.1016/j.celrep.2025.115483

[13] Chen R, Xu W, Sun Y, Zhi R, Xie P, Zhi Z, et al. 2-BFI Provides Neuroprotection Against Fluorosis by Stabilizing Endoplasmic Reticulum-Mitochondria Contact Sites and Inhibiting Activation of the NLRP3 Inflammasome. Neurochemical Research. 2023; 48: 591–603. https://doi.org/10.1007/s11064-022-03781-z

[14] Chen R, Zhao LD, Liu H, Li HH, Ren C, Zhang P, et al. Fluoride Induces Neuroinflammation and Alters Wnt Signaling Pathway in BV2 Microglial Cells. Inflammation. 2017; 40: 1123–1130. https://doi.org/10.1007/s10753-017-0556-y

[15] Hetz C, Zhang K, Kaufman RJ. Mechanisms, regulation and functions of the unfolded protein response. Nature Reviews. Molecular Cell Biology. 2020; 21: 421–438. https://doi.org/10.1038/s41580-020-0250-z

[16] Qian H, Zhao Y, Wang Y, Zhao H, Cui J, Wang Z, et al. ATR induces hepatic lipid metabolism disorder in rats by activating IRE1α/XBP1 signaling pathway. Toxicology. 2024; 501: 153696. https://doi.org/10.1016/j.tox.2023.153696

[17] Wang X, Xin H, Zhang C, Gu X, Hao Y. GRP94 Inhabits the Immortalized Porcine Hepatic Stellate Cells Apoptosis under Endoplasmic Reticulum Stress through Modulating the Expression of IGF-1 and Ubiquitin. International Journal of Molecular Sciences. 2022; 23: 14059. https://doi.org/10.3390/ijms232214059

[18] Peng YJ, Huang JJ, Wu HH, Hsieh HY, Wu CY, Chen SC, et al. Regulation of CLC-1 chloride channel biosynthesis by FKBP8 and Hsp90β. Scientific Reports. 2016; 6: 32444. https://doi.org/10.1038/srep32444

[19] Nkpaa KW, Onyeso GI. Rutin attenuates neurobehavioral deficits, oxidative stress, neuro-inflammation and apoptosis in fluoride treated rats. Neuroscience Letters. 2018; 682: 92–99. https://doi.org/10.1016/j.neulet.2018.06.023

[20] Liu B, Fu X, Du Y, Feng Z, Liu X, Li Z, et al. In Silico Analysis of Ferroptosis-Related Genes and Its Implication in Drug Prediction against Fluorosis. International Journal of Molecular Sciences. 2023; 24: 4221. https://doi.org/10.3390/ijms24044221

[21] Chen R, Yan L, Xie P, Tian J, Zhao Y, Liu Y, et al. Use of Diterpene Ginkgolides Meglumine Injection to Regulate Plasma Levels of PAI-1 and t-PA in Patients With Acute Atherosclerotic Cerebral Infarction. The Neurologist. 2022; 27: 299–303. https://doi.org/10.1097/NRL.0000000000000399

[22] Xiang J, Ma YL, Zou J, Zeng XX, Xiao X, Yu YL, et al. Extract of Ginkgo biloba leaves attenuates neurotoxic damages in rats and SH-SY5Y cells exposed to a high level of fluoride. Journal of Trace Elements in Medicine and Biology. 2023; 75: 127088. https://doi.org/10.1016/j.jtemb.2022.127088

[23] Zhang C, Ren C, Chen H, Geng R, Fan H, Zhao H, et al. The analog of Ginkgo biloba extract 761 is a protective factor of cognitive impairment induced by chronic fluorosis. Biological Trace Element Research. 2013; 153: 229–236. https://doi.org/10.1007/s12011-013-9645-4

[24] Berezutsky MA, Durnova NA, Andronova TA. Ginkgolide B:

mechanisms of neurobiological effects, prospects for use in the therapy of Alzheimer's disease. SS Korsakov Journal of Neurology and Psychiatry. 2024; 124: 22–27. https://doi.org/10.17116/jnevro202412404122 (In Russian)

[25] González-Alfonso WL, Pavel P, Karina HM, Del Razo LM, Sanchez-Peña LC, Zepeda A, et al. Chronic exposure to inorganic arsenic and fluoride induces redox imbalance, inhibits the transsulfuration pathway, and alters glutamate receptor expression in the brain, resulting in memory impairment in adult male mouse offspring. Archives of Toxicology. 2023; 97: 2371–2383. https://doi.org/10.1007/s00204-023-03556-7

[26] Cai Y, Zeng X, Wu M, Chen H, Sun M, Yang H. TET1 mitigates prenatal fluoride-induced cognition impairment by modulating Bcl2 DNA hydroxymethylation level. Molecular Medicine. 2025; 31: 117. https://doi.org/10.1186/s10020-025-01174-w

[27] Wang D, Cao L, Pan S, Wang G, Wang L, Cao N, et al. Sirt3-mediated mitochondrial dysfunction is involved in fluoride-induced cognitive deficits. Food and Chemical Toxicology. 2021; 158: 112665. https://doi.org/10.1016/j.fct.2021.112665

[28] Johnston NR, Strobel SA. Principles of fluoride toxicity and the cellular response: a review. Archives of Toxicology. 2020; 94: 1051–1069. https://doi.org/10.1007/s00204-020-02687-5

[29] Zhao H, Guo Q, Li B, Shi M. The Efficacy and Safety of Ginkgo Terpene Lactone Preparations in the Treatment of Ischemic Stroke: A Systematic Review and Meta-Analysis of Randomized Clinical Trials. Frontiers in Pharmacology. 2022; 13: 821937. https://doi.org/10.3389/fphar.2022.821937

[30] Zhou L, Gao Y, Lai XX, Xu TS, Yu M, Wang Y, et al. Post-marketing study on clinical safety of ginkgo diterpene lactone meglumine injection in 6300 patients with ischemic stroke. Zhongguo Zhong Yao Za Zhi. 2017; 42: 4744–4749. https://doi.org/10.19540/j.cnki.cjcmm.2017.0211

[31] Wei Q, Deng H, Cui H, Fang J, Zuo Z, Deng J, et al. A mini review of fluoride-induced apoptotic pathways. Environmental Science and Pollution Research International. 2018; 25: 33926–33935. https://doi.org/10.1007/s11356-018-3406-z

[32] Han X, Tang Y, Zhang Y, Zhang J, Hu Z, Xu W, et al. Impaired V-ATPase leads to increased lysosomal pH, results in disrupted lysosomal degradation and autophagic flux blockage, contributes to fluoride-induced developmental neurotoxicity. Ecotoxicology and Environmental Safety. 2022; 236: 113500. https://doi.org/10.1016/j.ecoenv.2022.113500

[33] Wen W, Zheng H, Li W, Huang G, Chen P, Zhu X, et al. Transcription factor EB: A potential integrated network regulator in metabolic-associated cardiac injury. Metabolism. 2023; 147: 155662. https://doi.org/10.1016/j.metabol.2023.155662

[34] Ratna A, Lim A, Li Z, Argemi J, Bataller R, Chiosis G, et al. Myeloid Endoplasmic Reticulum Resident Chaperone GP96 Facilitates Inflammation and Steatosis in Alcohol-Associated Liver Disease. Hepatology Communications. 2021; 5: 1165–1182. https://doi.org/10.1002/hep4.1713

[35] Kumari S, Dhapola R, Reddy DH. Apoptosis in Alzheimer's disease: insight into the signaling pathways and therapeutic avenues. Apoptosis. 2023; 28: 943–957. https://doi.org/10.1007/s10495-023-01848-y

[36] Liu R, Chen Y, Liu G, Li C, Song Y, Cao Z, et al. PI3K/AKT pathway as a key link modulates the multidrug resistance of cancers. Cell Death & Disease. 2020; 11: 797. https://doi.org/10.1038/s41419-020-02998-6

[37] Lo CH, Zeng J. Defective lysosomal acidification: a new prognostic marker and therapeutic target for neurodegenerative diseases. Translational Neurodegeneration. 2023; 12: 29. https://doi.org/10.1186/s40035-023-00362-0

[38] Majumdar A, Capetillo-Zarate E, Cruz D, Gouras GK, Maxfield FR. Degradation of Alzheimer's amyloid fibrils by microglia requires delivery of ClC-7 to lysosomes. Molecular Biology of the Cell. 2011; 22: 1664–1676. https://doi.org/10.1091/mbc.E10-09-0745